INSIGHT DERIVED FROM HIGH ORDER STRUCTURED FINITE DIFFERENCE CFD SIMULATIONS OF FLOW PAST GENERIC SIMPLIFIED CAR MODELS

by

Maxwell L. Henry

A thesis submitted to the faculty of
The University of North Carolina at Charlotte
in partial fulfillment of the requirements
for the degree of Master of Science in
Mechanical Engineering

Charlotte

2016

Approved by:

Dr. Mesbah Uddin

Dr. Peter T. Tkacik

Dr. Praveen Ramaprabhu

ABSTRACT

MAXWELL L. HENRY. Insight derived from high order structured finite difference CFD simulations of flow past generic simplified car models.
(Under the direction of DR. MESBAH UDDIN)

This thesis focuses upon using a high-order finite-difference method on a structured overset grid to study flow features around a generic simplified car model adjusting mesh refinements, rear slant angles, solvers, and turbulence models. These processes are explored to develop a procedure for simulating more complex and realistic car models. Three different mesh refinements from 17 to 108 million vertices were tested with three different solvers (RANS, URANS, and DES) on an Ahmed body with subcritical slant angle to ascertain the optimum mesh parameters for subsequent simulations. Using a 57 x 10^6 vertices mesh, multiple rear slant angles near the critical angle ($\phi = 30°$) were investigated with RANS and URANS approaches to compare C_D, C_L, and flow fields with experimental and CFD found in literature. Similar trends were observed in CFD predictions and experimental data, including flow separation at the critical angle ($\phi = 30°$), but all predicted results were within 15% of experimental measurements for both time-averaged and unsteady simulations. At the sub-critical angle (25°), CFD predictions using multiple hybrid RANS/LES approaches were compared against time-averaged and unsteady experimental measurements. These did not disagree with previous results and C_D values were over predicted by a maximum of 4% while C_L values were under predicted by a maximum of 15% when compared to experimental results. Subsequent studies investigating elongated mesh refinement areas were inconclusive. The procedures outlined compare reasonably well to experimental data and can be used as a starting point for simulating more realistic models including complex dynamic pitch, heave, and roll simulations involving road vehicles.

DEDICATION

To my parents, girlfriend, and greyhound for all of the support they have given throughout this process.

ACKNOWLEDGEMENTS

I would like to thank my advisor, Dr. Mesbah Uddin, for his guidance and insights into the problem throughout this entire project. I am thankful for being able to bounce ideas and concepts off of fellow students Brett Peters and Alex Curley. Their individual insights into the use of OVERFLOW has been a life saver at times. Finally, I would like to thank Mike J. Lucas at Ingersoll Rand for introducing me to OVERFLOW and CFD in general over three years ago. Without that introduction and summer of cavity acoustics research, this project would have never been realized.

TABLE OF CONTENTS

LIST OF FIGURES

LIST OF TABLES

CHAPTER 1: INTRODUCTION

Computational Fluid Dynamics (CFD) is a rapidly growing field, intertwined with the development of computer hardware and software alike. In recent years, the gains in these capabilities have allowed industries, large and small, to use CFD to design and develop new complex products quicker, easier, and cheaper. The ability to numerically solve problems involving fluid flow reduce dependence on physical testing, which can be an expensive process. Numerical modelling also allows CFD users to measure phenomena without affecting the overall simulation and get an unparalleled insight into fluid flow that would be impossible with conventional testing methods. These characteristics give CFD the ability to be a powerful tool, but as with all tools, CFD currently has its limitations.

The inability to analytically solve the Navier-Stokes equations forces all fluid flow problems to require the need to be numerically solved. While the discretization process of these equations is straight forward, the necessary resolution to resolve all scales of turbulent fluid flow is beyond the current computational capabilities except for very simple shapes at low Reynolds numbers. Modelling turbulence alleviates the need to resolve the computational domain at Kolmogorov scales, but this modelling means no single turbulence model correctly predicts the fluid flow or body forces for all possible flow configurations. The multitude of turbulence models available demands intimate knowledge of their functionality and limitations in order to implement them correctly within CFD simulations and to provide accurate conclusions about the fluid flow.

An industry where CFD is gaining traction as a predictive tool is the automotive industry, where testing and development of new vehicles is expensive and time con-

suming. Related to the automotive industry, where CFD is being increasingly used at all professional levels, is the motorsports industry. CFD helps provide additional testing abilities in a sport where design optimization is of paramount importance and the regulations limit the use of expensive wind tunnels. Race teams are consistently turning towards CFD as a preliminary design tool for more in-depth analysis of the flow field that wind tunnel testing is unable to provide.

While no method of simulating real world phenomena is perfect, the limitations of CFD neither give the confidence, nor the full predictive capabilities in order to be a perfect substitute for wind tunnel testing. Multiple examples within motorsports can be given where race teams eliminated wind tunnel testing and failed to reap the benefits of modelling solely with CFD.

In order to rectify this issue, computational methods have to be thoroughly tested and researched for the full benefits of CFD to be realized. Among other shortfalls, CFD fails to accurately predict body forces on simple objects without an aspect of the flow being forced to exemplify the observed characteristics or models being tuned for an extremely specific circumstance.

The motivation for investigating a simple body on a high-order overset structured grid is to expand these techniques to other, more complicated and realistic problems. While other CFD codes can apply boundary conditions and other methods to model the complicated physics, overset grids can actively move within the simulation giving a transient view of the motions. Overset grids easily lend themselves to incorporate moving meshes without requiring morphing the mesh. The high-order solver method coupled with high-order interpolation between overset grids within OVERFLOW allows for highly accurate solutions for complicated geometry that is unavailable for other codes. The methods within this thesis can easily be expanded to more complicated models that incorporate rotating wheels and actively moving aerodynamic components. Instead of having a quasi-steady simulation of a moving airfoil, over-

set grids can actively move the airfoil and directly view the transient effects of these motions. Motorsports teams are actively looking toward these methods to model dynamic actions on the race track, such as how the aerodynamic elements perform when the car pitches under breaking or rolls during turns. Currently these transient effects are not well observed and can lead to large performance gains.

This thesis investigates using a high-order finite-difference method on a structured overset grid to study the flow around a generic simplified car model to provide a better understanding of the flow around ground vehicles. It also provides a different direction towards a method for better predictions of forces for these simplified objects with the goal of applying them to more complex and realistic models incorporating moving meshes.

1.1 Organization of Thesis

Chapter 1 indicated the motivations for this thesis and provided a basic structure the thesis will follow.

Chapter 2 looks at different types of geometry to be simulated in order obtain the objectives of this thesis. Previous research and experiments are also discussed within this section.

Chapter 3 provides information on the finite-difference code used to solve the subsequent simulations as well as how the generic simplified car model was meshed, how boundary conditions were chosen, and how the simulation was setup in order to run. Turbulence modelling information is also provided within this section.

Chapter 4 contains the results and discussion of various simulations. These include choosing the optimal grid size using the Grid Convergence Index (GCI), changing the rear slant angle, changing the solver method, and looking at a different turbulence model. These simulations look at how the body forces and vortex shedding changes with modifying geometry and models and how they could be improved.

Chapter 5 concludes all sections and provides future directions subsequent studies

could provide.

CHAPTER 2: SOLVING THE PROBLEM

2.1 What Geometry Should Be Simulated?

Simulating automotive flows is an extremely complex problem due to the multiple interactions that are basic necessities for these problems. A simple automotive model needs to simulate the road, rotating wheels, a radiator, and small components that affect the flow field such as side mirrors and door handles. Modelling a simple motorsports vehicle requires even more complexity due to the numerous aerodynamic elements essential to its function. Figure 2.1 shows the complexity of flow around an open-wheeled race car. These additional complexities do not include physics modelling, which is made more difficult due to the high speeds achieved by these vehicles. These projected models, while simplified from realistic scale models, are still incredibly complex and deviate from the flow observed on the track and in the wind tunnel. While the ultimate goal is to be able to model these flows, building an accurate model will be a time intensive process and may still fail to correctly model the physics of the flow due to a lack of fundamental understanding about the physics of the flow.

Simplified automotive models, such as the DrivAer geometry [21], are popular due to their realism, which include essential characteristics of consumer-bound vehicles (Figure 2.2). The original experiment released data made available to the public in order for other parties to verify their findings and correlate with CFD. Investigation of unsteady flows around these more complex bodies, until recently, was only feasible for major manufacturers, where there were enough computational resources to model these bodies and plenty of confidential experimental data to confirm the results. The continual advances in computational technology allows for relatively inexpensive re-

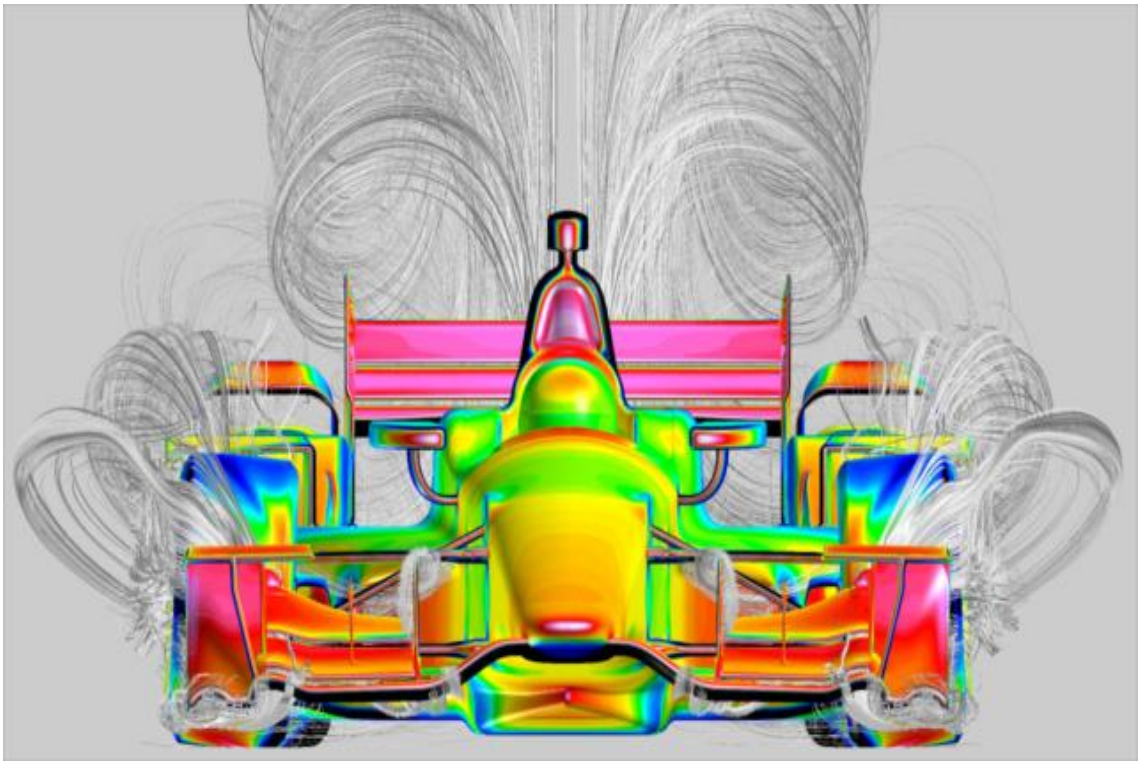

Figure 2.1: Streamlines around Chevrolet's 2015 IndyCar bodykit[63]

sources to run simulations large enough to resolve small intricacies of the flows around these realistic bodies. While these new simulations are approaching or exceeding 100 million cells and are predicting trends similar to experimental data, the complex flows and interactions are still not being reproduced properly due to the inability to model the entire spectrum of turbulent scales[4][52].

In order to resolve these flows, simpler models must be used to answer questions about the fundamental characteristics of the flow. More simplified generic car models include the Windsor model [51] and SAE Reference model [60], which are much simpler than the DrivAer model, but still retain some complexity of the flow, such as familiar automotive shapes or rotating wheels including spoilers, fenders, and hoods (Figures 2.3 and 2.4). Even with these generic simplified car models complexity of the flow still presents problems in modelling and predicting the finer elements. One of the problems with these larger models is the inability to achieve mesh sizes that are truly

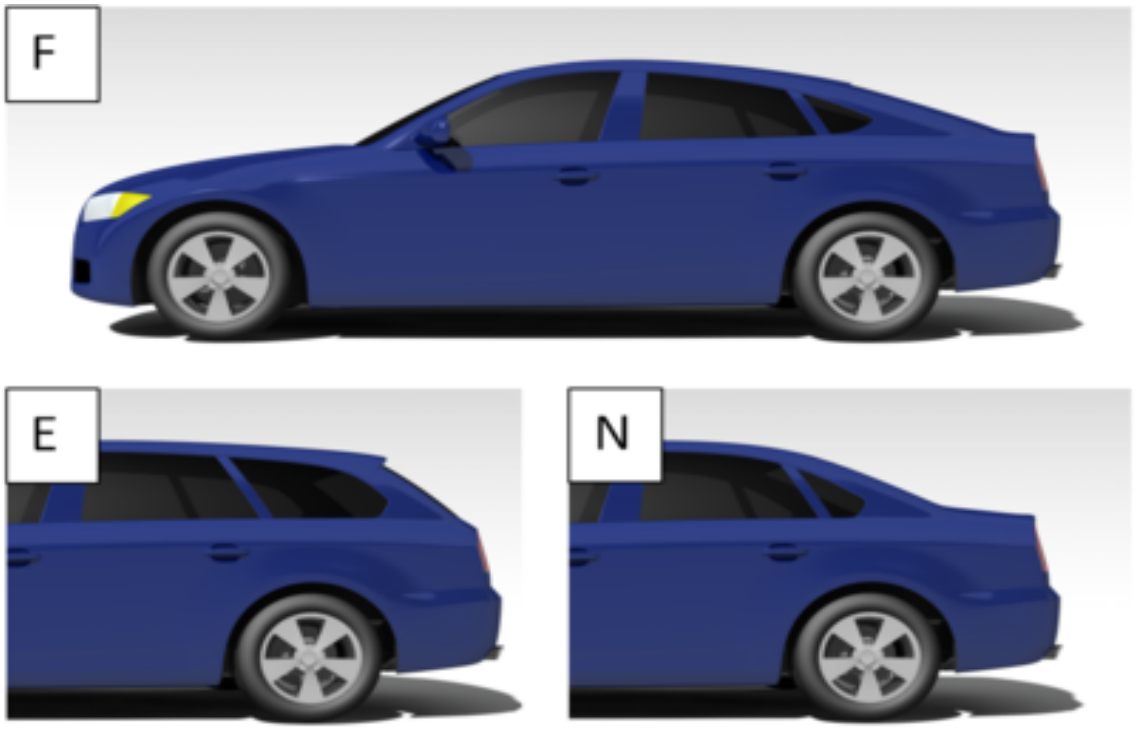

Figure 2.2: Image of the DrivAer model [4]

grid independent. Minute changes to discretization settings can lead to counts of drag to increase or decrease without actual changes to the physics of the flow.

Attempting to find a solution to improving the CFD predictions of road vehicle aerodynamics does not have to revert back to the flow of simple bluff bodies and geometrical shapes. These shapes are simple enough that direct numerical simulation (DNS) can be used to a high degree of accuracy. A simple generic simplified car model that has been simulated via CFD since its creation is the Ahmed reference model, which was a variation of the simpler Morel model [2][38]. The Ahmed reference model is more complex than cubes or spheres and is a parallelepiped with rounded edges oriented towards the direction of the flow with a slanted rear face (Figure 2.5).

The varying characteristic of the Ahmed body is the angle the rear face deviates from the top of the model (ϕ), which affects the behavior of the wake. Major characteristics of the flow include recirculation behind the body, flow separation from the

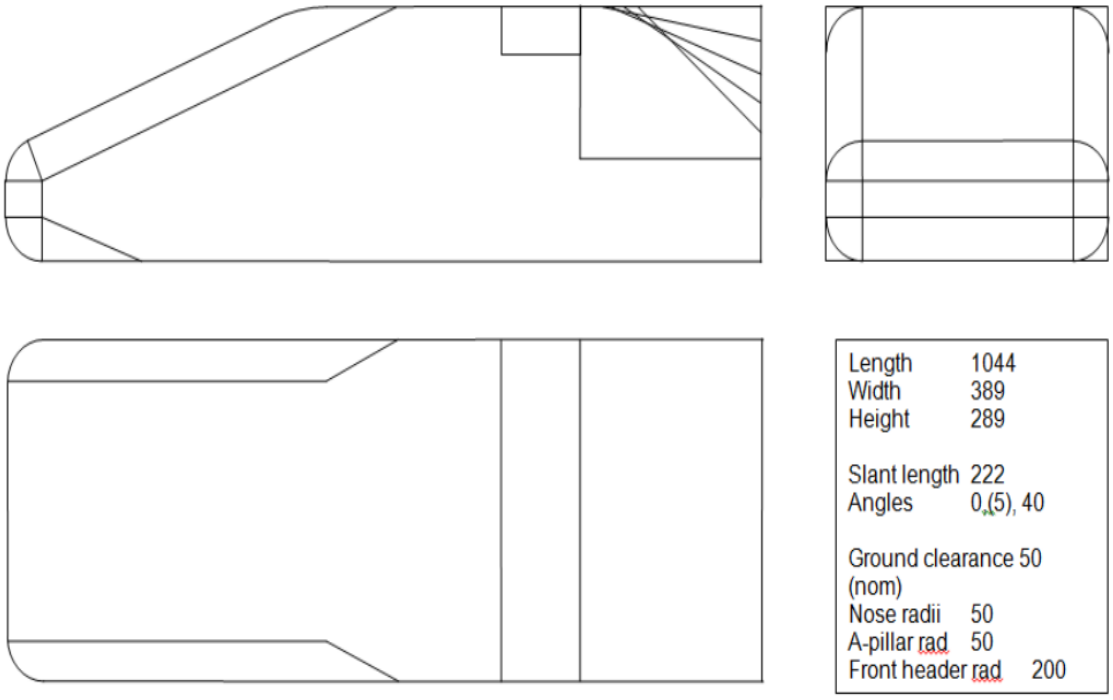

Figure 2.3: Dimensions and shape of the Windsor Reference Body [51]

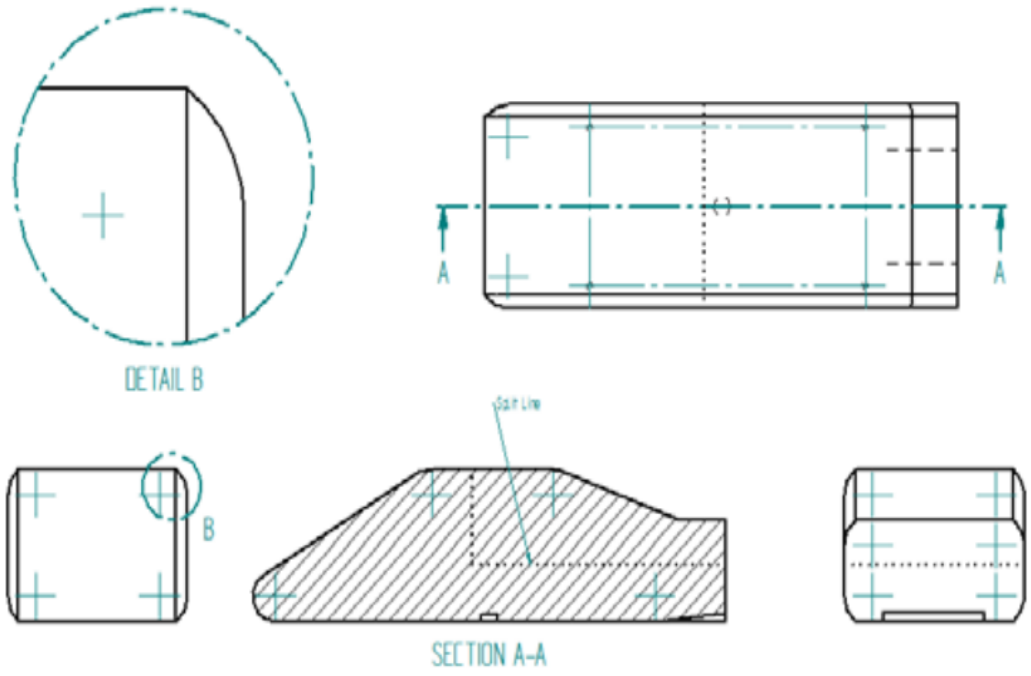

Figure 2.4: Dimensions and shape of the SAE Reference Model [60]

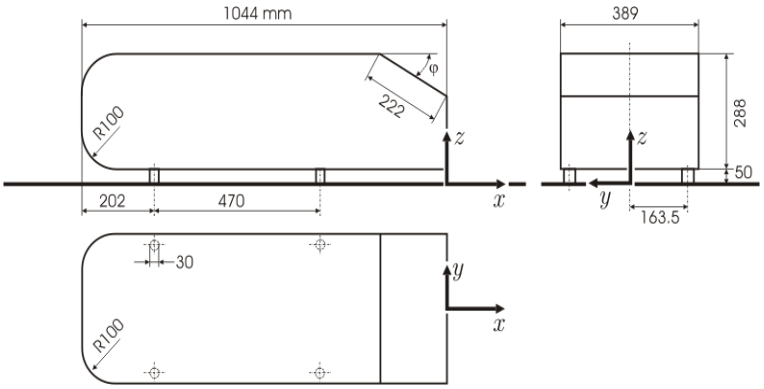

Figure 2.5: Dimensions of the Ahmed Body [2]

rear slant, and vortices generated by the rear slant, all large flow features that affect modern vehicles. While the Ahmed body is a relatively simple shape, the minor flow characteristics are not simple at all. Multiple horseshoe vortices along the upper surface of the body, vortex shedding within recirculation zones, and vortices produced along the length of the body are a few to name. A full schematic of the complexity of this problem is shown in Figure 2.6, but one needs to remember that this flow field is much simpler to model than the fully realistic race car flow field. The vortices and flow separation are intricacies that turbulence models struggle to predict and limiting the number of complex features allows for a better understanding of the underlying physics of the flow.

Due to the quantity of information available on the Ahmed body and the relative simplicity of the model, a computer model created within the CAD software Pro/E was chosen to perform subsequent simulations around the critical, sub-critical, and supercritical angles. Even with the simplicity of the flow, the Ahmed body is continually chosen to test new computational methods and experimental measuring equipment due to its predictability and well documented results.

2.2 Experiments

The original experiment with the Ahmed body was performed at 60 m/s for a Reynolds number based upon length of 4.29 x 10^6[2]. Within this experiment 85% of

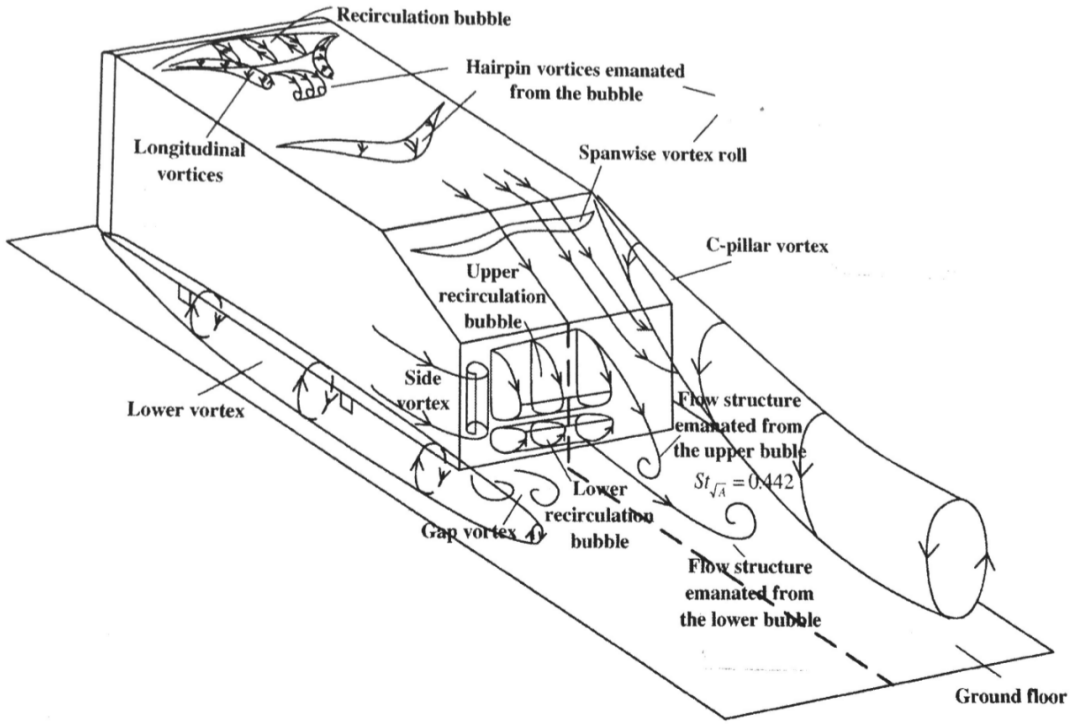

Figure 2.6: Flow characteristics of the Ahmed Body[61]

the drag was attributed to pressure drag therefore pressure recovery translated into lower drag coefficients. As the rear slant angle was increased from 0 to 40 degrees, a critical angle of 30° was observed where the drag coefficient dramatically increased to a maximum of 0.378 (high drag configuration) before completely separating from the rear slant and dropping to a decreased value of 0.260 (low drag configuration)(Figure 2.7). The high drag configuration was the original body with no adjustments, where the low drag configuration was produced by fixing a splitter plate vertically on the symmetry plane 25 mm behind the model to help trip the flow into completely separating [2]. Even though the original experiment did not report lift coefficients, an additional experiment replicated these results and reported C_L values for the various angles, but did not include a low drag configuration [7].

Since the original experiment was performed, numerous follow up studies have been performed both in CFD and within the wind tunnel. Most of these experiments

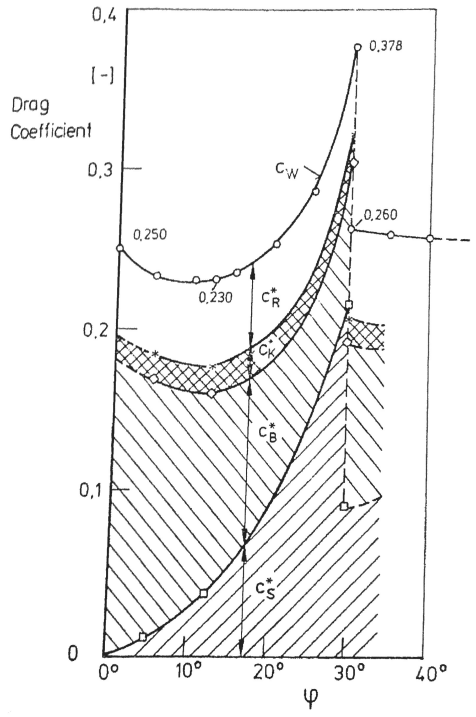

Figure 2.7: Variation of C_D as a function of ϕ for the original Ahmed body experiment[2]

focus upon the critical angle ($\phi = 30°$), sub-critical angle ($\phi = 25°$), and super-critical angle ($\phi = 35°$). These angles produce flows that can be tripped into high or low drag configurations at the critical angle, flow that separates and reattaches along the rear slant at the sub-critical angle, and flow that completely separates at the super-critical angle.

Leinhart performed a PIV experiment of the Ahmed body at the sub and super-critical angles[29]. Their experiment was performed at 40 m/s due to the limitations of the wind tunnel resulting in a Reynolds number based upon length of 2.29 x 10^6[28]. While the bulk flow velocity did not match the original experiment, the Reynolds number was comparable to the experiment by Ahmed and it was argued that it would not considerably affect the flow physics of the problem.

Current topics of interest is the spectral signature of the separations from the Ahmed body since these minor changes can increase efficiency margins for road vehi-

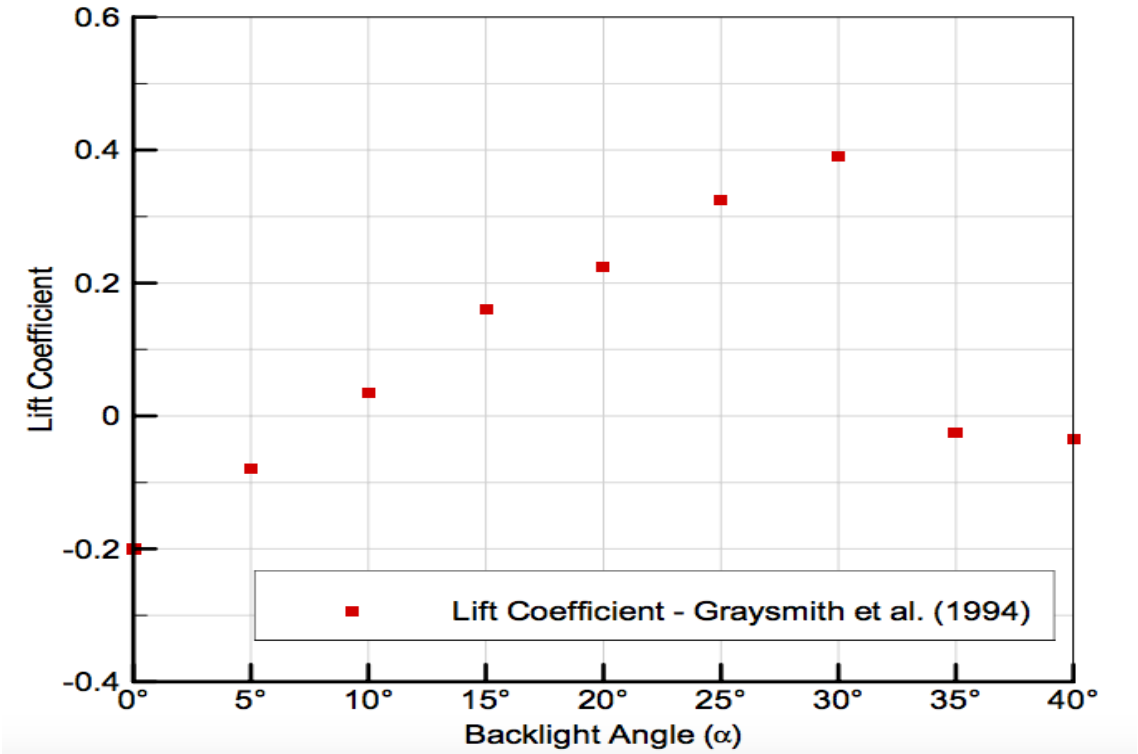

Figure 2.8: Variation of C_L as a function of ϕ for a subsequent wind tunnel study on the Ahmed Body[7]

cles. Thacker and Zheng performed experiments to specifically look at these characteristics within the wake. Resolving these minor changes can allow for active control over the frequency at which they separate, resulting in more control over drag and lift characteristics[54][61]. Thacker's experiment replicated that of Leinhart and was performed looking at the sub-critical angle of $\phi = 25°$ predicting a Strouhal number of 0.2 at the rear slant[54]. Zheng's experiment was performed at a much lower Reynolds number due to the low speed (8.33 m/s @ Re = 56,000) and third scale model used for the experiments [61]. This experiment also looked at the shedding of vortices around every minor aspect of the Ahmed body in an attempt to quantify and reduce the uncertainty within other experimental measurements since reported values were rarely consistent.

These experiments are drawn upon the create a CFD simulation with specific flow features being investigated in order to improve the accuracy of low-speed vehicle

aerodynamic simulations.

CHAPTER 3: SIMULATION ESSENTIALS

3.1 What Code to Use?

There are two main methods of discretizing a fluid domain, finite-volume and finite-difference; each of which have their own benefits and drawbacks. The finite-volume method discretizes the fluid domain into discrete volumes in which the fluid flow equations are solved. Volume integrals of partial differential equations are evaluated as fluxes at the surface of each finite volume through the use of the divergence theorem. Due to the information connectivity between the adjacent volumes being transferred by the fluxes through the volumes, finite-volume methods are inherently conservative and follow all conservation laws. The information transfer of conservative variables ensures that only miniscule numerical errors result in mass discrepancies. Another benefit of finite-volume methods is that they are solved on unstructured grids, where the orientation of volumes within the grid does not have to have set coordinates and only connectivity information is necessary. This allows for easily created meshes that can be any number of polyhedral shapes, ultimately helping to optimize the performance of the mesh.

Both of these characteristics mean that they are prime candidates for most commercial CFD software. Software such as OpenFOAM, CD-Adaptco's STAR-CCM+, and Ansys' Fluent use these finite-volume methods. Most of these finite-volume methods use 2nd order solvers [5], which means results can be produced reasonably accurately and quickly, prime characteristics that are attractive to industries. The fast paced motorsport industry demands these characteristics since gaining small incremental performance bonuses quicker than the competition can lead to winning or

losing.

Most of the CFD research that the subsequent studies are compared to uses the finite-volume approach to gain insights into the solutions, but are consistently inaccurate. While inaccuracy ranges from 5 to 10%, there is a small portion of the flow physics that is not getting resolved with these methods. One of the problems with finite-volume approaches is that high order solvers are much more complicated than other discretization methods and therefore only 2nd order solvers are readily available. As industries turn towards CFD for its efficiency and predictive capabilities, the small portion of flow physics that is not getting resolved can lead to inconsistent and deceiving predictions for the flow field. Research is being done for higher order methods, but currently these methods are extremely time consuming and resource intensive[31].

Alternatively, finite-difference methods discretize the fluid domain into nodes where the fluid equations are solved. The differential equations are solved with, as the name suggests, difference equations assuming the base equations are well behaved. Taylor series expansion form the backbone of high-order methods and infinitely higher order methods can eventually be obtained with enough patience as shown in Equation (3.1) [14]. Within this equation d is the desired derivative to approximate, p is the order of desire accuracy, and h is the grid spacing.

$$F^{(d)}(x) = \frac{d!}{h^d} \sum_{n=0}^{d+p+1} \left(\sum_{i=i_{min}}^{i_{max}} i^n C_i \right) \frac{h^n}{n!} F^{(n)}(x) + O(h^p) \tag{3.1}$$

In order for Equation (3.1) to be satisfied it is necessary that

$$\sum_{i=i_{min}}^{i_{max}} i^n C_i = \left\{ \begin{array}{l} 0,\ 0 \leq n \leq d+p-1 \text{ and } n \neq d \\ 1,\ \text{n = d} \end{array} \right\} \tag{3.2}$$

Within this generic equation *forward difference approximation* is when $i_{min} = 0$ and $i_{max} = d + p - 1$, *backward difference approximation* is when $i_{min} = -(d + p - 1)$

and $i_{max} = 0$, and finally *centered difference approximation* is when $i_{max} = i_{min} = (d + p - 1)/2$ [14].

Even though higher orders of accuracy are more computationally intense, the overall number of calculations are less than those of the finite-volume methods of equal orders of accuracy. Used primarily in research, finite-difference methods are on structured grids that do not require the connectivity information of finite-volume methods and are therefore less memory intensive. Interest of this method has come from the motorsports industry since the higher orders of accuracy show promising results.

An added benefit of structured grids is the ability to integrate overset meshes, where multiple structured grids are overlapped and high-order interpolation methods are used to transfer information between grids. These overset meshes can include active aerodynamic changes instead of rigid bodies. Rotating wheels, vibrating wings, and other complex geometries can be incorporated with relative ease, since each individual component is meshed and dynamic movements are added afterwards. A current use of this method is in the aerospace industry where individual helicopter rotor blades are meshed and can reactively move according to the aerodynamic forces they experience [40]. Without the overset mesh capability, total forces on the helicopter and aeroacoustic frequencies are nearly impossible to resolve. Coupled with the high-order solvers, these methods mitigate the effects of not following conservation laws, but there is a finite simulation time that can be achieved before simulation results diverge from reality. These methods are used within the flow solver OVERFLOW, a code developed by NASA primarily for evaluating the flow around the Space Shuttle [40]. Due to reduced research within this area of discretization methods, increased orders of accuracy, and reduced memory needs, the study of flow around a generic simplified car model will be with the finite-difference methods found within OVERFLOW.

3.2 OVERFLOW

OVERFLOW solves the time-dependent, Reynolds-averaged, Navier-Stokes equations, is fully compressible in all three dimensions, and an open source code. A secondary motivation to use OVERFLOW was the open source element, where additional boundary conditions, turbulence models, and solvers can easily be added and tested. While this aspect of the code was not expanded upon within the current study, learning how to operate the code correctly was a subsequent result of this research.

The primary motivation of using OVERFLOW was its built in capabilities to use 6th order spatial finite-difference solvers and 2nd order temporal finite-difference solvers, coupled along with multiple different turbulence models and basic boundary conditions.

OVERFLOW was developed for high Mach and transonic flows around aircraft, but the flexibility of these models allows the software to perform well at low Mach numbers near the incompressible range, such as those within many aerodynamic simulations. This forces the code to use Low-Mach preconditioning methods in order to avoid sever stability restrictions on the time steps [42].

3.3 Meshing

Chimera Grid Tools (CGT) was an additional software package that was suggested to be used in conjunction with OVERFLOW. Within CGT are grid generation, pre and post processing, and visualization tools, which are tailored for OVERFLOW and other overset grid systems. Generating the surface mesh could have been done solely through CGT due to the simple geometry, but a model had already been constructed through Pro/E and was imported into CGT for its major curves to be extracted. All subsequent model changes were made via CGT.

The main issue with receiving good results starts with the mesh quality of the simulation. Without a quality mesh the simulation will not return dependable results

to make any definitive statements about the physics of the flow. The importance of the mesh meant some time was taken to carefully follow best practices as well as understand the flow that was to be expected to custom tailor a mesh to accurately help solve the problem.

For the structured mesh there are two different areas of meshing to focus upon; surface and volume meshing. A poor quality surface mesh will lead to a poor quality volume mesh as the mesh is extended into the flow field where as a poor quality volume mesh will reduce the effects of a perfect surface mesh since information will not be correctly transmitted from the far field to the wall. The surface mesh was created using best practices from Chan *et. al.*[11]. These guidelines were used to not only optimize the overset meshes used, but to ensure the volume mesh that was generated would be of a high quality.

3.3.1 Preliminary Calculations before Building Mesh

Since there is turbulence modelling, the value of the wall y^+ is important to ensure that flow at the boundary is correctly predicted, an important characteristic for this flow. While the actual value of the wall y^+ can only be viewed after the simulation has completed, the actual definition of the wall y^+ is used to approximate a distance for the first node where ρ_ω is density at the wall, u^* is the flow velocity at the first node, y is the first node distance from the wall and μ_ω is viscosity at the wall as shown in equation (3.3) [11]. The following steps were used as advised by [11] to find the wall y^+

$$y^+ = \frac{\rho_\omega u^* y}{\mu_\omega} \tag{3.3}$$

Assuming $\rho_\omega = \rho_\infty$ and $\mu_\omega = \mu_\infty$ the y^+ and wall distance equations can be rewritten as a function of Reynolds number and skin friction coefficient.

$$y^+ = Re\sqrt{\frac{c_f}{2}y} \tag{3.4}$$

$$y = \frac{y_+}{Re\sqrt{\frac{c_f}{2}}} \tag{3.5}$$

where c_f is the skin friction coefficient. It is acceptable for this to be estimated from the flat-plate correlation's from "Viscous Fluid Flow"[59] which is:

$$c_f \approx \frac{0.455}{\ln\left(0.06Re_x\right)^2} \tag{3.6}$$

where $Re_x = 0.1Re$. Since OVERFLOW is a compressible code, even though the speeds that were to be run are extremely low, well within the incompressible range, the compressibility of the flow was considered only to be consistent with other simulations run with this code and to be consistent with the code's internal calculations of wall y^+. The compressibility factor (f_{comp}) is shown as a relationship of the bulk flow Mach number

$$f_{comp} = 1 + 0.1157M_\infty^2 \tag{3.7}$$

which is used to correct the Reynolds number for the compressibility effect

$$r_{comp} = \frac{1}{\frac{\mu^*}{\mu_\infty}f_{comp}} \tag{3.8}$$

Using Sutherland's law, the viscosity and compressibility correction is computed for the Reynolds number with $S = 199°R$ for air so that the compressible skin friction can be calculated as

$$c_f \approx \frac{0.455}{ln^2(0.06Re_x r_{comp})f_{comp}} \tag{3.9}$$

The difference between the free stream and wall conditions can be summed up as

the following equations by the relationships shown above

$$\frac{\mu^{\omega}}{\mu_{\infty}} = \left(\frac{T^{\omega}}{T_{\infty}}\right)^{\frac{3}{2}} \left(\frac{1+\frac{S}{T_{\infty}}}{\frac{T^{\omega}}{T_{\infty}}+\frac{S}{T_{\infty}}}\right) \tag{3.10}$$

$$\frac{T^{\omega}}{T_{\infty}} = 1 + \frac{\gamma-1}{2} Pr^{\frac{1}{3}} M_{\infty}^{2} \tag{3.11}$$

$$\frac{\rho_{\omega}}{\rho_{\infty}} = \left(\frac{T^{\omega}}{T_{\infty}}\right)^{-1} \tag{3.12}$$

Finally, a modified expression for the distance to the wall can be written accounting for the minor compressibility effects of the fluid flow, which can be written as

$$y = \frac{y_{+}}{Re\sqrt{\frac{c_f}{2}}} \left(\frac{\frac{\mu^{*}}{\mu_{\infty}}}{\sqrt{\frac{\rho_{\omega}}{\rho_{\infty}}}}\right) \tag{3.13}$$

Aiming for $y^{+} < 1$ the estimated value for the first node distance is $y < 0.124$ mm to simplify this the first node distance used below is 0.1 mm.

3.3.2 Building the Mesh

The body of the geometry was split into seven different overlapping sections for surface and volume meshes to be created from these parts. Each face was given its own separate overlapping grid with the top and rear slant of the geometry being split into two separate entities allowing easy changes to the rear slant angle. Each foot peg was also its on separate overlapping grid with collar grids being made between the body and the floor in order to align the simulations with the "Best Practices" for overlapping grid creations [11].

All of the surface grids had a stretching ratio across the plane of 1.05 with the wall spacing at the corners 0.1 mm. As in the original experiment, the separation behind the generic automotive body is an important area to ensure mesh quality since the changing wake structure affects the drag of the body. This region as well as the region

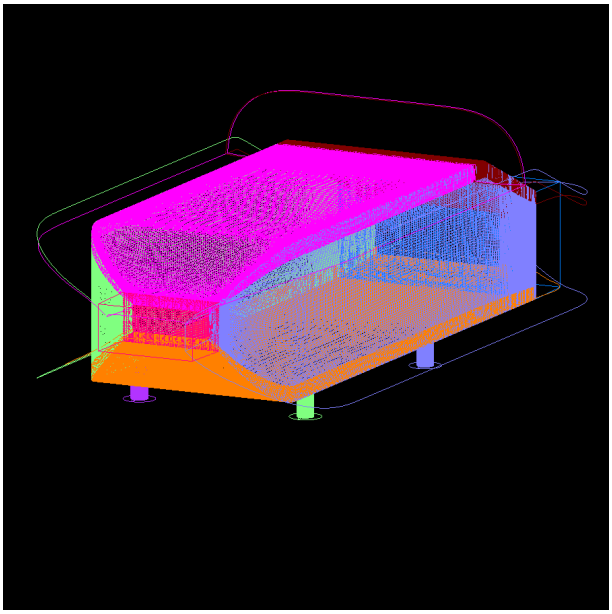

Figure 3.1: Surface and volume grid of generic simplified car model

on the slant of the body has to be refined more intensely than the other regions in order to help predict the correct angle where the flow separates. This region had a stretching ratio of 1.01 to increase the resolution within this area.

Growing the volumes from the surface mesh were trivial and were very easy due to the simplicity of the base geometry and careful overlapping within the surface mesh. The stretching ratio for growing the surface in the normal direction was 1.01 and the surfaces were grown for a distance of 100 mm where possible to ensure not only adequate capturing of the boundary layer as it developed along the body, but also to help the connectivity between the off body overset grids. The "Best Practices" guide "suggests that 20 to 30 points in the boundary layer is considered good resolution," the resulting points used within this baseline simulation is 51 points to ensure a good overlap with other off body grids[11]. The additional points did not require too much additional computational resources and were necessary to ensure connectivity between the surface and off body grids. The surface and volume grids of the body are shown in Figures 3.1 and 3.2.

The area where these parameters of the surface mesh were not possible were the

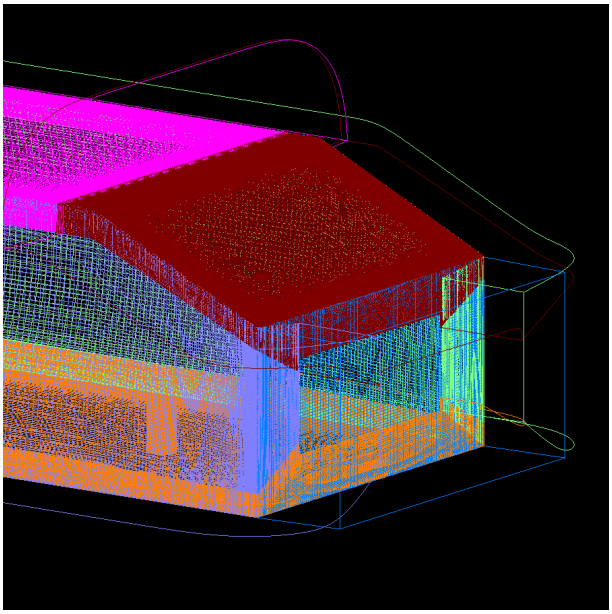

Figure 3.2: Close up of modularity of rear slant overset grid

underbody region. The underbody and feet need to be appropriately refined in order to avoid creating errors by failing to model the turbulence created within this region. The flow in this region, especially on the downwind side of the feet, is extremely turbulent which could affect the wake; therefore, care also had to be taken within these regions as well. The ground clearance was only 50 mm and the geometry of the foot pegs did not allow for the previous growth distance. The underbody region was grown nearly to the floor (49 mm), with the same stretching ratio as before, to ensure complete coverage under the body and to ensure perfect connectivity with the other volume regions on the body. The foot pegs were grown normal to their respective surfaces for 35 mm, with the same stretching ratio as before, but an off body doughnut was placed around the foot peg to ensure connectivity between the feet, underbody grid, and the floor grid due to the mismatch between the three final cell sizes. This arrangement allowed for minimal orphan points to be created. Orphan points are created when there are not enough nodes overlapping for the high-order interpolation methods. The order of interpolation method is reduced around these regions during the calculations of the flow. Too many orphan points can lead to solutions diverging and being unable

to produce a reliable solution. Only 300 orphan points were created around each foot, just four thousandths of a percent of the nodes within the underbody region could not use 5th order grid to grid interpolation methods. These orphan points made up an even small portion of the entire grid as a whole. All of the volume grids near the geometry had a first node distance of 0.1 mm from the wall.

Creating off body grid was much easier since only Cartesian grids were used. In an effort to reduce computational expense, only the off body grids close to the geometry resolved the boundary layer. The width of this domain was 3 meters, exactly the same width as the nozzle within the wind tunnel. Seven Cartesian off body grids were used within this portion of mesh creation (Figure 3.3). Two grids were used to cover the body with one across the entire body and and a half body length of the wake (5 mm node spacing), while the other was a more refined grid covering only the rear slant and a half body length of the wake (2.5 mm node spacing) as shown in Figure 3.5. The additional grids covered front, rear, sides, and top of the geometry (5 mm node spacing). Only the grids touching the floor were refined near the floor to capture the boundary layer. The first node distance of 0.1 mm and stretching ratio of 1.01 was also used for these regions up to 50 mm above the floor, where the 5 mm constant node spacing was resumed (Figure 3.3). These grids started a full body length before the model and extended two body lengths beyond the end of the model.

In order to ensure that the pressure gradient near the boundary of the simulation was negligible, the computational domain had to be large enough to prevent the boundary conditions from affecting the flow. After some trial and error, a computational domain of Γ = 13.4 L x 11 W x 9.4 H was chosen as the best option for further simulations, similar to the ERCOFTAC recommended dimensions [48]. In choosing the computational domain, multiple RANS simulations with the exact same discretization setup were carried out until the drag predictions do not depend upon the domain size. Five overset grids were used to fill the remaining portions of the

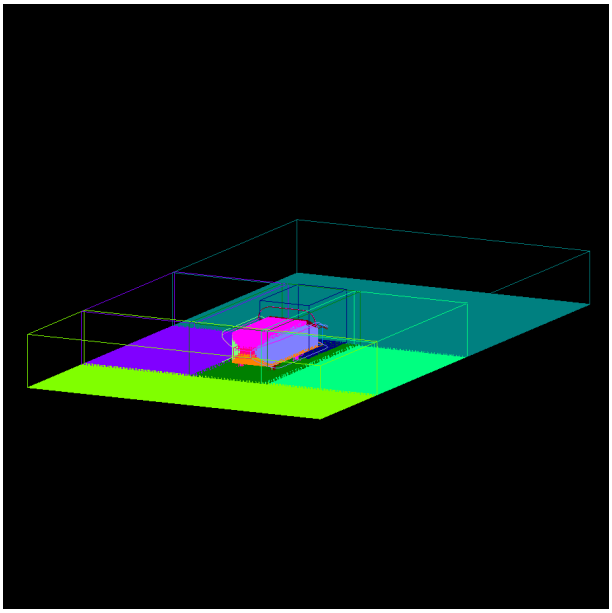

Figure 3.3: Off Body Cartesian grids used to refine immediate area around body. These grids were refined on the floor to resolve the boundary layer

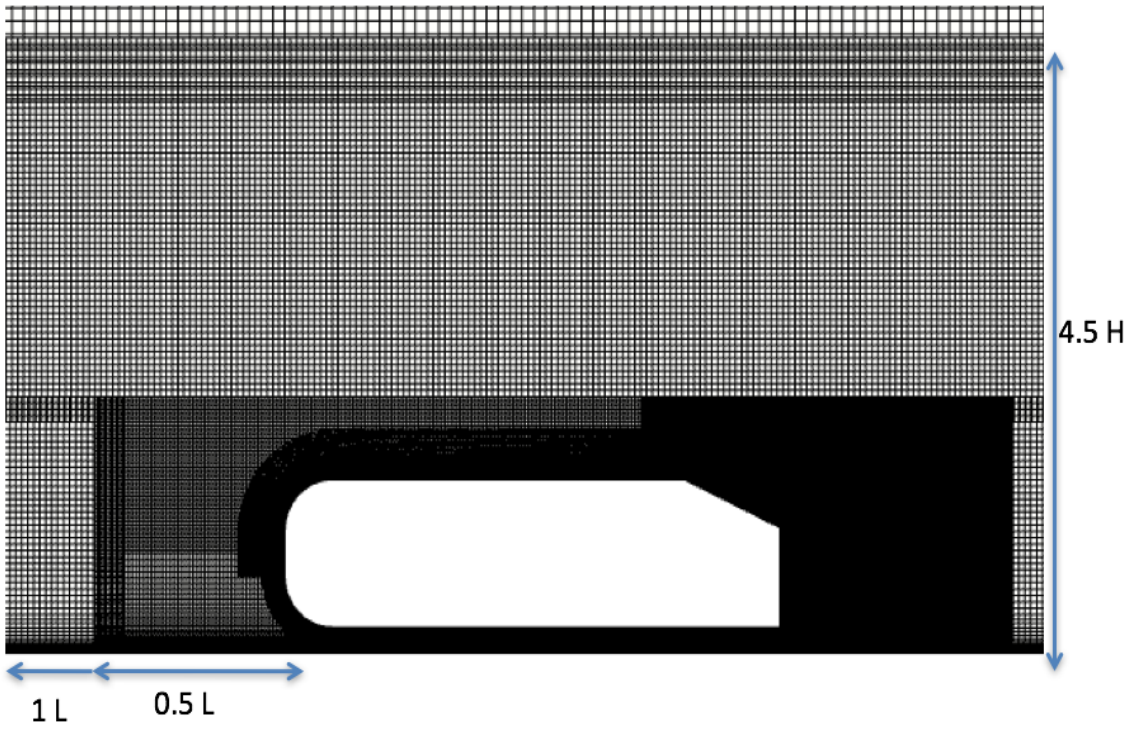

Figure 3.4: Close Up of the mesh around the symmetry plane of Y = 0 highlighting the refinements around the body

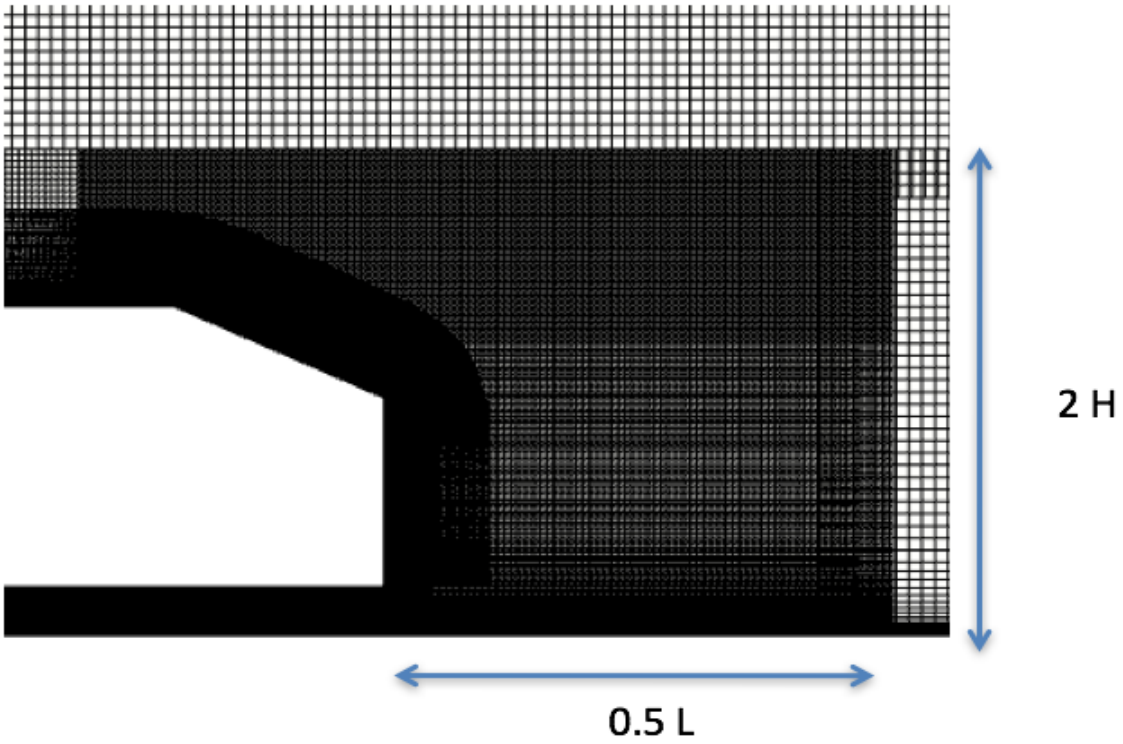

Figure 3.5: Close Up of the mesh around the symmetry plane of Y = 0 highlighting the dimensions of the refinements

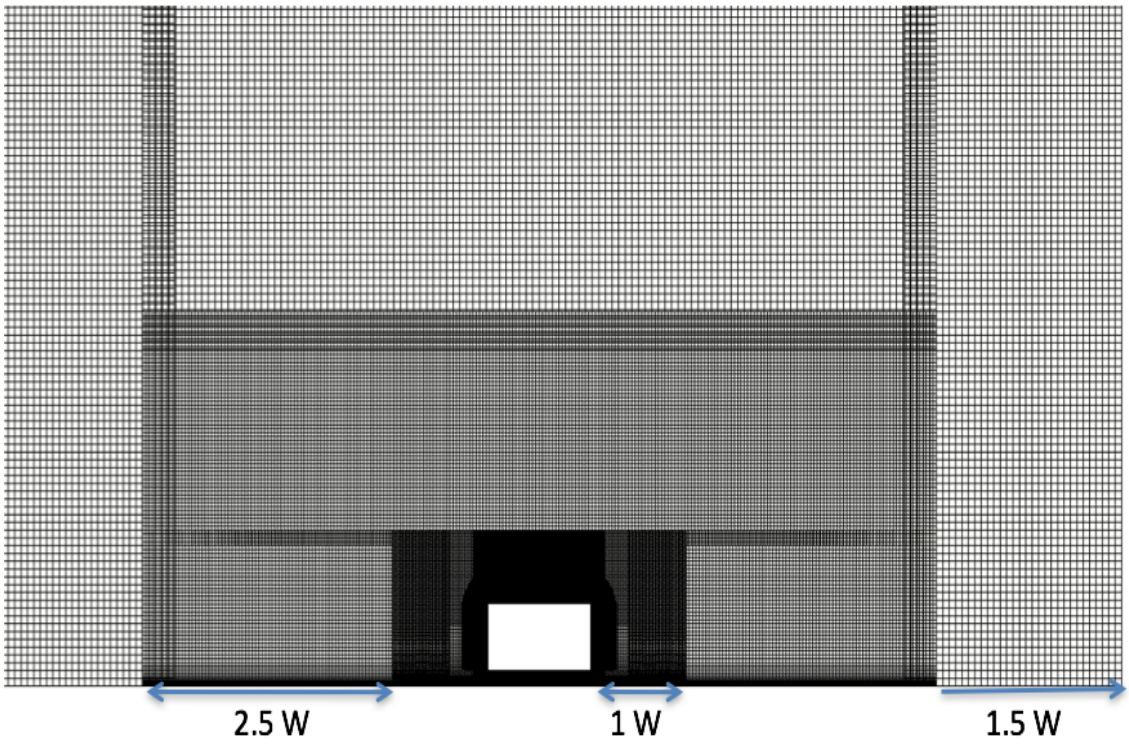

Figure 3.6: View of the mesh around x = 1000 highlighting the dimensions of the grid

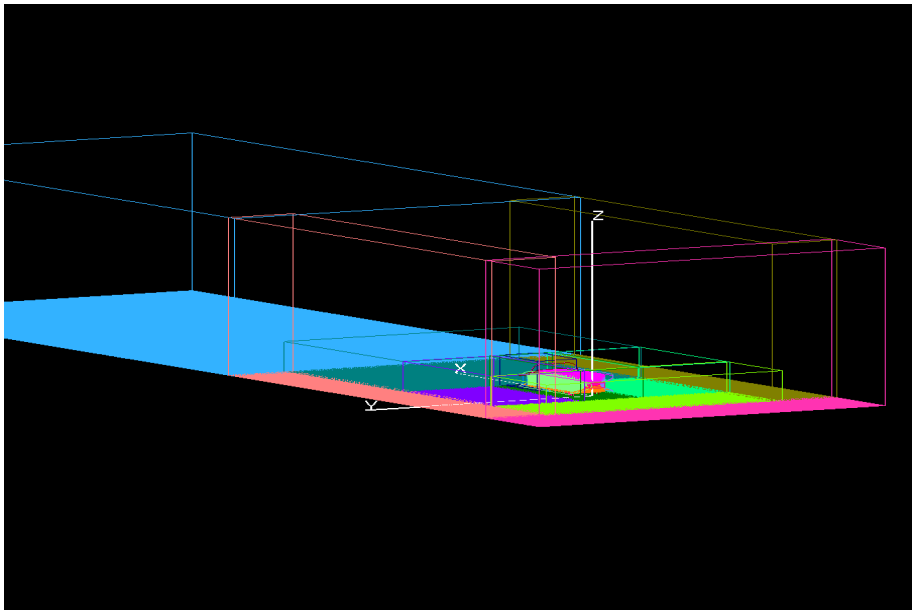

Figure 3.7: Off Body Cartesian grids used to refine immediate area around body

computational domain and making up the inlet, outlet, and side boundaries where the overall node spacing is 10 mm (Figure 3.7).

From this baseline grid there were only two modifications; changing the rear slant angle and creating a larger off body grid to refine the wake. Changing the rear slant angle required only adjustments of the vertical position of the rear corners according to the specific angle and rebuilding the surface and volume mesh of the rear slant. Since this was a structured overset grids, modifying the simulations only required removing the old rear slant geometry and adding the new rear slant geometry. The refined wake region was extended an entire body length in an effort to increase the resolution of the wake as it decayed.

3.3.3 Boundary Conditions

The boundary condition specification is just as important as the mesh setup due to the ability of the boundary conditions to propagate through the domain. Incorrect or misused boundary conditions will affect the ability of the mesh to return accurate and reliable results. The boundary conditions chosen for this simulation are the simplest

preset boundary conditions within OVERFLOW to make the simulation easy to setup.

For simplicity the inlet and outlet boundary conditions are a velocity inlet and pressure outlet. Excluding the floor of the computational domain, the remaining boundaries are all set to the free stream flow speed. It would be more correct to use a symmetry play boundary condition to eliminate the possibility of pressure information from reflecting back into the simulation, but the computational domain is large enough that the pressure gradient is negligible at the boundaries.

The far field off body Cartesian grids were not refined near the floor to reduce computational expense and it would be improper to have a viscous wall describe the floor of the grids since the boundary layer would not be correctly resolved. In these outer regions the floor was described as an inviscid wall preventing a boundary layer from being created at these locations. Ensuring the correct prediction of the boundary layer, a viscous wall boundary condition describes all interior grids. The boundary layer starts to grow a full body length before the simulated model and has fully formed before interacting with the model.

3.4 Simulation Setup

The basic setup of each simulation is relatively simple since there are no moving parts and the geometry is simple enough to define with one basic boundary condition. For each simulation the inlet velocity is set to 40 m/s or Mach 0.114575, which means the free stream boundaries are also at this velocity. This velocity was used by Leinhart *et. al.* and consequently most other authors simulating this geometry followed suit[62]. Other than this initialization setting the basic initial conditions are the same as the conditions of an ideal gas at sea level (ρ = 1.229 kg/m^3 and μ = 1.73 x 10^{-5}N$\cdot$ s / m^2). While these do not exactly reflect the experimental values, they will not have a significant impact upon the results of the simulation.

Most of the other settings used to begin the simulation are related to the numerical and turbulence models used. The goal of these simulations is to simulate a generic

car model with high orders of accuracy. The spatial and temporal orders of accuracy are 5^{th} and 2^{nd} order respectively while code the was compiled using double precision.

The time derivatives are dealt with the 2nd order implicit backward differentiation formula (BDF2), which is of the family of backward differentiation formula methods. The backward differentiation formulas are an implicit method that requires the solution to the non-linear equations at each time step[3]. These methods are solved using a variation of Newton's method and there are 15 subiterations between each time step to receive an adequate approximation. OVERFLOW users suggest using 30 to 50 subiterations for proper convergence, but to reduce computation time 15 subiterations are used[11]. The residuals during this number of subiterations are near complete convergence before moving to the next time step. The initial solution is accurate enough that the relatively small number of Newton subiterations does not significantly affect the solution.

The numerical scheme for the spatial derivatives was the 5^{th} order finite-difference (Weighted Essentially Non-Oscillatory) WENO upwind algorithm[49]. The high order WENO scheme was used due to its ability to preserve vortices throughout the domain with reduced numerical diffusion[49]. The low Mach numbers of the simulation reduce the chance of discontinuous solutions arising therefore non-physical solutions are less likely to occur. Due to lack of shocks within the resulting simulations, the low numerical diffusion is ideal to accurately preserve flow features.

For all of these simulations a Courant number, from the Courant-Friedrichs-Lewey condition (CFL), of 4 was used to drastically speed up the computational time of the simulation. The CFL number is chosen based upon the stability of the equations to be solved. A CFL number of 1 corresponds to the solution advancing with the smallest mesh scale within the simulation, when CFL ≥ 1 the solution advances faster than the smallest mesh scale, and when CFL ≤ 1 the solution advances slower. Higher CFL numbers allow the solution to be completed quicker at the risk of diverging,

while lower CFL numbers are stable, but take much longer. Due to the size of the simulations, a higher CFL number was preferred to reduce months of computational time into weeks. For these simulations a CFL number of 4 is not optimized, but small simulations indicated this value corresponded to a conservative value for stability.

Within the code there are many options to increase the convergence of the solution. These methods either initialize and run on coarser grids for a preset number of iterations before moving to finer grids or have large smoothing coefficients for easy convergence. The only smoothing coefficients used to slightly ease the convergence were the default smoothing coefficients for 2^{nd} and 4^{th} order terms. Ultimately future grids should be appropriately refined and allow for these smoothing coefficients to be zero. The compressibility of the code allows for low-speed regions to be smoothed during transonic simulations, but for a simulation as slow as the subsequent studies it would ruin the ability to receive any relevant results since most of the changes to the overall flow field happen in the low-speed wake region. Within these low-speed regions, predetermined by the code, the speed of sound (c) is replaced by $\frac{M}{M_\infty}$ to minimize smoothing within each local region therefore improving the accuracy of the solution [42][23].

All of the unsteady simulations were started from a previous steady-state simulation. Starting with a converged steady-state solution helped increase the convergence wall-clock times of every unsteady simulation. The time to run a complete simulation from zero seconds until full convergence would take three times as long without using the steady state converged solution. While there were no unsteady simulations started without pre-converged solutions, the transient solution quickly disappeared and it is assumed that it did not affect the overall outcome of each simulation. Each simulation ran for 0.1 seconds, or 4 complete passes across the body. More passes across the body was desired, but time limitations demanded an optimum number of time steps allowable in order to complete the full study.

3.4.1 Turbulence Modelling

The major parameter that was changed within the physics of this study was the turbulence model. All simulations used variations of the Menter SST model with the symmetric successive over relaxation (SSOR) as a preconditioner for the involved matrices. Tied into this turbulence model are settings for the Reynolds-Averaged Navier-Stokes model (RANS), Unsteady Reynolds-Averaged Navier-Stokes model (URANS), Detached Eddy Simulation model (DES), Delayed-Detached Eddy Simulation model (DDES), and Multi-Scale models that were also tested and indicated within the initialization file. Additionally, the Spalart-Allmaras DDES model was used to compare to one simulation.

Turbulence models have been used to bridge the gap between the ability to solve the Navier-Stokes equations directly and modelling fluid flow by simpler methods. Most turbulence models solve a turbulent kinetic energy term (k), and a term to define the length scale of turbulence. Currently the most popular method for two-equation turbulence models have been to solve for turbulent specific dissipation (ω) instead of just turbulent dissipation (ϵ) as in the $k-\epsilon$ models [12]. All of the turbulence models used within this study assume the Boussinesq approximation, where the Reynolds stresses, τ_{ij}, are linearly proportional to the velocity gradients, $\frac{\partial u_k}{\partial x_k}$, through the rate-of-strain tensor, S_{ij} (Eq (3.14)). From this relationship the eddy-viscosity, μ_t, can be obtained for the respective turbulence model[40].

$$\tau_{ij} = 2\mu_t\left(S_{ij} - \frac{1}{3}\frac{\partial u_k}{\partial x_k}\delta_{ij}\right) - \frac{2}{3}\rho k\delta_{ij} \tag{3.14}$$

The $k-\epsilon$ model works very well within shear flows and the far field, but fails in the near-wall region, which would make them inaccurate and undesirable to predict body forces [12]. Since the near wall region is where the body forces are being generated $k-\omega$ models are much more useful within this region [12]. Unfortunately, $k-\omega$ models

are susceptible to the free stream value for ω, which is not only hard to accurately obtain, but also its value dramatically affects the simulation [12]. In order to counter the opposites of these two turbulence models, Menter proposed forming a turbulence model that blended the two models in such a way that the near wall $k-\omega$ was the model chosen to simulate turbulence and as the flow reached the far-field, the $k-\epsilon$ model simulated the flow [12].

As shown below, the Equations (3.15) and (3.16) solve for the turbulent kinetic energy and specific dissipation for the Baseline SST model,

$$\frac{\partial(\rho k)}{\partial t}+\frac{\partial(\rho u_j k)}{\partial x_j}=P-\beta^*\rho\omega k+\frac{\partial}{\partial x_j}\left[(\mu+\sigma_k\mu_t)\frac{\partial k}{\partial x_j}\right] \tag{3.15}$$

$$\frac{\partial(\rho\omega)}{\partial t}+\frac{\partial(\rho u_j\omega)}{\partial x_j}=\frac{\gamma}{\nu_t}P-\beta\rho\omega^2+\frac{\partial}{\partial x_j}\left[(\mu+\sigma_\omega\mu_t)\frac{\partial\omega}{\partial x_j}\right]+2(1-F_1)\frac{\rho\sigma_{\omega 2}}{\omega}\frac{\partial k}{\partial x_j}\frac{\partial\omega}{\partial x_j} \tag{3.16}$$

while the production and dissipation terms are shown in Equations (3.17) and (3.18)

$$P=\tau_{ij}\frac{\partial u_i}{\partial x_j} \tag{3.17}$$

$$\tau_{ij}=\mu_t\left(2S_{ij}-\frac{2}{3}\frac{\partial u_k}{\partial x_k}\right)-\frac{2}{3}\rho k\delta_{ij} \tag{3.18}$$

followed by the shear stress and eddy viscosity equations (Equations (3.19) and (3.20)).

$$S_{ij}=\frac{1}{2}\left(\frac{\partial u_i}{\partial x_j}+\frac{\partial u_j}{\partial x_i}\right) \tag{3.19}$$

$$\mu_t=\frac{\rho a_1 k}{\max\left(a_1\omega,\Omega F_2\right)} \tag{3.20}$$

With the best characteristics of the $k-\omega$ and $k-\epsilon$ models the SST model should

perform extremely well in the near-wall region and in the far-field, which is mostly true. The SST model has known issues within adverse pressure gradients and tends to separate early due to the calibration of the eddy-viscosity term[15][34]. Small corrections to the a_1 coefficient within Equation (3.20) have helped correct this issue, but for this study the original formulation of the SST model have remained unchanged for validation of this method[35]. Additional characteristics of the SST model are that it tends to over predict the extent of the separation area and does not line up with the pressure recovery seen within experiments [35].

3.4.2 Need for Formulations of hybrid RANS-LES models

It is well cited and shown within previous simulations that RANS turbulence models over damp the unsteady motion of the flow ultimately affecting the extent and effect the wake has on the flow field[53][36][50]. This inherent ability of RANS turbulence models is due to the assumption that they are able to resolve all scales of the flow [53]. As the smaller scales became more resolved, the predicted solution became a better approximation of the final solution. The Richard Extrapolation exercise, demonstrated in Chapter 4, shows this effect by essentially resolving all scales of the flow by approximating the continuum values [43]. Within hybrid RANS/LES models the RANS portion is extremely refined near the wall in order to capture the smaller scales, but further from the wall there is a transition to solving the LES equations at scales that can be appropriately resolved with a reasonable level of mesh refinement. The major difference between these hybrid RANS/LES models is the blending or damping function between the RANS and LES switch.

The modification to the SST model for Detached-Eddy Simulation (DES) is to replace the dissipation term with

$$\epsilon = \frac{\omega}{\beta^* k} = \frac{k^{2/3}}{\min(L_t, C_{DES} L_g)} \tag{3.21}$$

where the blending function between the $k-\epsilon$ and $k-\omega$ portions of model becomes

$$C_{DES} = (1 - F_1)C_{DESKE} + F_1 C_{DESKW} \tag{3.22}$$

with $C_{DESKE} = 0.61$ and $C_{DESKW} = 0.78$ [53]. With this formulation the turbulent dissipation is increased when the grid scale is less than the turbulent scale, an inherent problem with the SST-DES model since it vastly overestimates the dissipation. Correcting for this overestimate means other models can be used instead, such as a multi-scale model, which damps dynamic viscosity at the junction between RANS and LES domains, or the Delayed Detached-Eddy Simulation (DDES) model which transitions from RANS to LES domains as a function of the ratio of the local turbulent length scales and grid spacing effectively delaying the effect of dissipation when compared to the DES formulation[40].

3.5 Vortex Identification

The main flow features of the generic simplified car model used is the vortices that are produced around the body. Viewing and identifying vortices within an experiment is much easier than mathematically identifying these vortices since there are many ways to define vortices [22]. A common way to identify vortices is through vorticity, which is defined as the curl of the velocity as shown in Equation (3.23).

$$\omega = \nabla \times \mathbf{V} \tag{3.23}$$

While this method will always show vortices due to the increased changes in velocity around a vortex core, it will also highlight different characteristics of the flow. The magnitude of vorticity will dramatically increase near a wall due to the increased changes in the velocity field due to a boundary layer. Vortices near the wall may be difficult to identify near the wall due to this effect.

In order to reduce the uncertainty of vortex identification near the wall, the λ_2

criterion looks for a pressure minimum without the effects of unsteady straining and viscosity [22]. This reduces the vortex identification method into looking at the rate-of-strain tensor (Equation (3.24)) and the vorticity tensor (Equation (3.25))[20].

$$\mathbf{S} = \frac{1}{2}[\nabla v + (\nabla v)^T] \tag{3.24}$$

$$\mathbf{Q} = \frac{1}{2}[\nabla v - (\nabla v)^T] \tag{3.25}$$

The vortex identification comes from the eigenvalues of $\mathbf{S}^2 + \mathbf{Q}^2$ where $\lambda_2 < 0$ [24]. This method ensures that the low pressure core of vortices is identified, but the boundary of the vortex is still ambiguous. λ_2 is generally reported in negative values where as $|\lambda_2|$ increases the identified vortex increases in size, which may not be physically accurate [20].

These two methods are the main methods used within this thesis. While this is not an exhaustive list of vortex identification methods, using both in conjunction with each other allows for an adequate interpretation of how the vortices are formed and appear within the flow.

CHAPTER 4: RESULTS AND DISCUSSION

4.1 Grid Convergence Index

The problem that was simulated is very complex and can only be numerically solved to achieve a solution unlike simple 2D or 3D problems where an exact solution can be derived and error easily obtained. More complex problems, especially large CFD simulations, do not have this luxury and numerous sources of potential error can contribute to a large degree of uncertainty in the solution. One solution to identify the uncertainty within the solution is the Grid Convergence Index (GCI), evaluated by Roache, and it has become a popular way to determine the discretization error [43].

The GCI method assumes that grid refinements will lead to a more accurate solution and additional refinements will allow the solution to be asymptotically converting to the exact solution. Both of these assumptions are reasonable for solutions that are averaged over a length of time similar in the method used to gain data within experiments. The method is mathematically based upon the theory of generalized Richardson Extrapolation where k_0 is the unknown rate of convergence, h, h/t, and h/s are three distinct step sizes. The unknown rate of convergence is only found numerically with Equation (4.1) after the solution A has been determined making this method *posteriori*[43].

$$A = \frac{t^{p_0} A(\frac{h}{t}) - A(h)}{t^{p_0} - 1} + O(h^{p_1}) = \frac{s^{p0} A(\frac{h}{s}) - A(h)}{s^{p0} - 1} + O(h^{p_1}) \tag{4.1}$$

Equation (4.1) allows for finding solutions at an increased resolution meaning at minimum only one coarse simulation needs to be completed for a better solution to

be predicted at an increased resolution. For finding the discretization error between successively refined grids means that at least two, but ideally three, simulations to be finished for the method to work accurately and effectively. The logarithmic relationship between the error (E) induced by the grid and the grid spacing (h) as well as the order of accuracy of the actual grid (p) is shown below in (4.2), with C being an offset constant,

$$\ln E(h) = \ln C + p \ln h \tag{4.2}$$

As shown by Roache, the refinement ratios only need to be larger than 1.3 to obtain good results when using GCI[43]. With a non-constant mesh refinement, equation (4.2) can be written three times and solved for the order of convergence (p) to correspond to the three different grids that were tested[46].

$$p = \frac{|\ln|\frac{f_{32}}{f_{21}}| + q(p)|}{\ln r_{21}} \tag{4.3}$$

$$q(p) = \ln\left(\frac{r^{p_{21}} - 2}{r^{p_{32}} - s}\right) \tag{4.4}$$

$$s = -\left(\frac{f_{32}}{f_{21}}\right) \tag{4.5}$$

The equations (4.3),(4.4), and (4.5) can be solved iteratively using an initial guess of $q(p) = 0$, which corresponds to a constant grid refinement ratio.

The last step to using the GCI method is to find the 'continuum' solution using Richardson Extrapolation where there is no spacing between the grid points ($\Delta h = 0$). For Equation (4.6), the two largest grids are used and the order of convergence found through the iterative solution of Equations (4.3), (4.4), (4.5).

Table 4.1: GCI results and errors for RANS simulations at all levels of resolution

Grid Size x 10^6	C_D	C_L
107.9	0.299 ±0.0001	0.291 ±0.0001
57.3	0.302 ±0.001	0.274 ±0.001
17.1	0.273 ±0.010	0.209 ±0.008

$$f_{\Delta h=0} \approx f_1 + \frac{(f_1 - f_2)}{(r^p - 1)} \tag{4.6}$$

The GCI therefore provides the estimate of the finest grid solution relative to the converged numerical solution ($\Delta h = 0$).

$$GCI_{21} = \frac{F_S e_{21}}{r^{p_{21}} - 1} \tag{4.7}$$

$$e_{21} = \left| \frac{(f_2 - f_1)}{f_1} \right| \tag{4.8}$$

where F_S is the 'safety factor' and e_{21} is the relative error term. For three or more grids it is advised to use a $F_S = 1.25$ and for two grids it is advised to use $F_S = 3$. The F_S term corresponds to a 95% confidence interval [46].

In the interest of time and following the 'Best Practices' of overset meshing, the meshes that were constructed do not have uniform grid spacing or a constant refinement ratio [11]. The geometry used within this portion of the study had a rear slant angle of $\phi = 25°$. The coarsest mesh used had 17.6 x 10^6 vertices, the finest mesh had 107.9 x 10^6 vertices, and a medium mesh had 57.2 x 10^6 vertices. These grid refinements were chosen through a previous study as the best representations of a spectrum of grids. With these three grids RANS, URANS, and DES simulations were performed and the results would determine the level of refinement used for additional studies. This assumes that even if the rear slant angle changes or turbulence model changes the overall error will not considerably change.

Table 4.2: GCI results and errors for URANS simulations at all levels of resolution

Grid Size x 10^6	C_D	C_L
107.9	0.301 ±0.001	0.305 ±0.001
57.3	0.302 ±0.005	0.283 ±0.004
17.1	0.274 ±0.025	0.152 ±0.014

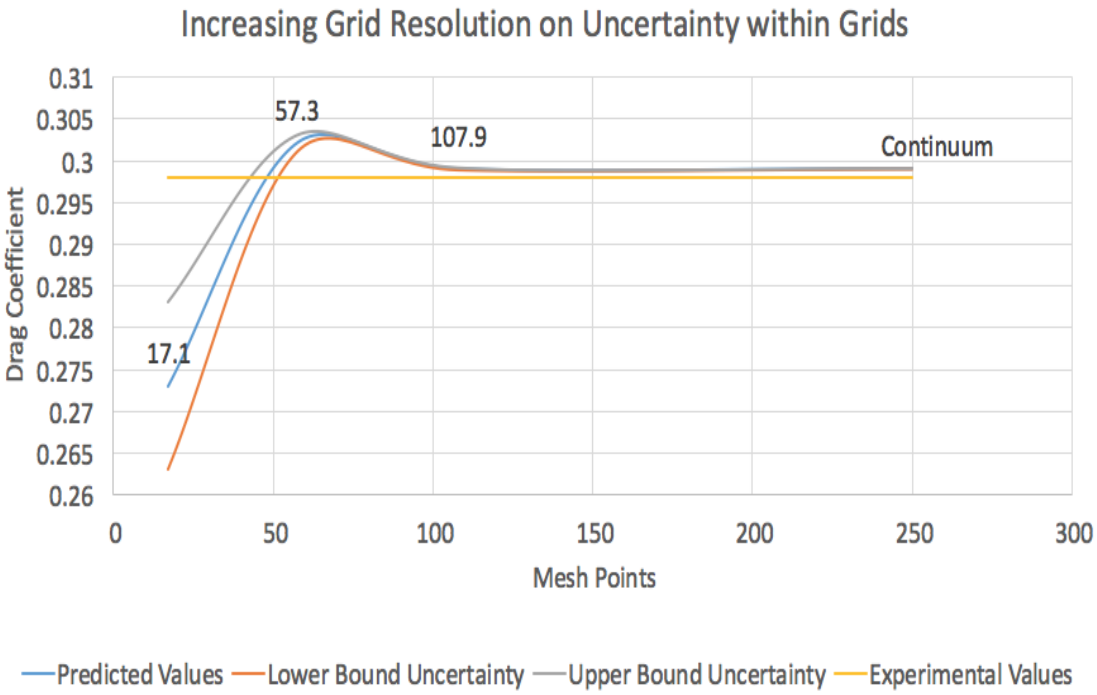

Figure 4.1: Graph of convergence as number of nodes increases to approximated continuum value for RANS C_D values

As shown in tables 4.1 and 4.2, the errors of the simulations increase as the solving method becomes more complex. This is expected due to the failure to resolve the finer scales that are modelled. Even though the finer scales are not being resolved as well, the overall trend of finer meshes predicting more accurate results is consistent. Extrapolating from the two DES simulations, the finest grid is predicted to have an error of only 2.3 %, which would mean the errors between CFD predictions and experimental measurements would overlap.

Viewing the graphs (Figures 4.1, 4.2, 4.3, 4.6), the rates of convergence appear to be logarithmic, a basic assumption of the GCI process, and that the values at the 107.9

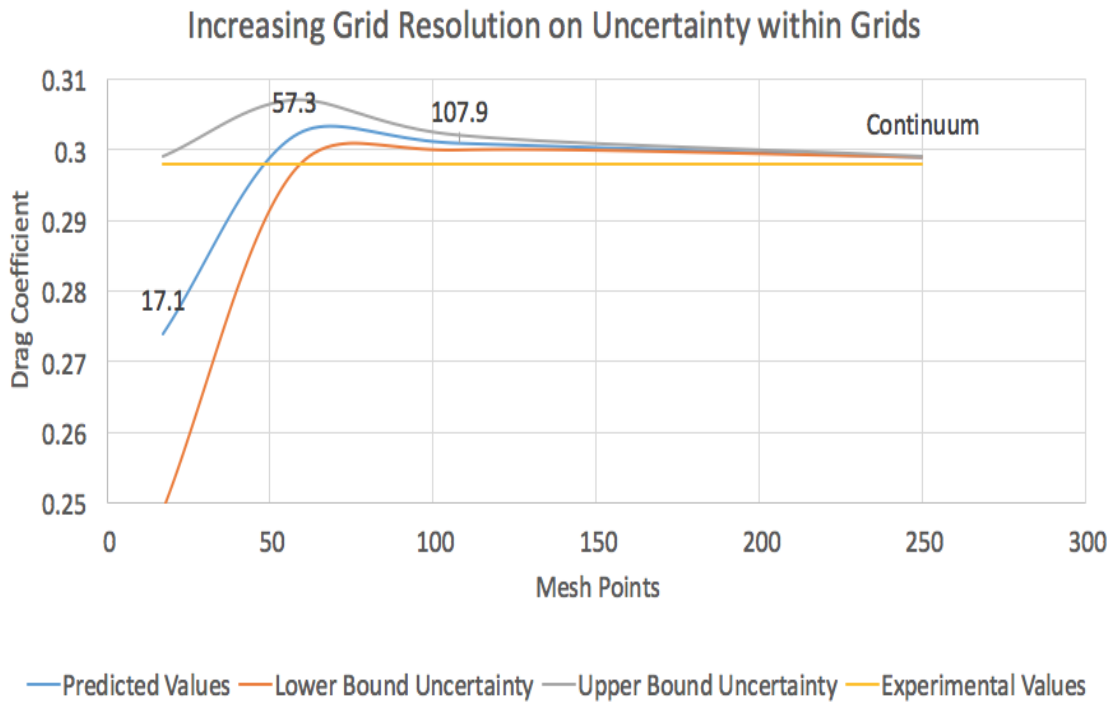

Figure 4.2: Graph of convergence as number of nodes increases to approximated continuum value for URANS C_D values

Table 4.3: GCI results for DES simulations at coarse and medium resolutions

Grid Size x 10^6	C_D	C_L
57.3	0.309 $\pm$0.022	0.270 $\pm$0.019
17.1	0.252 $\pm$0.058	0.107 $\pm$0.025

x 10^6 mesh size are nearly converged when compared to the 'Continuum' value, when the grid spacing (h) approaches zero. C_D and C_L both appear to be converged by the medium grid, with some uncertainty even though the most refined grid gives the most accurate answers. The convergence graph of the DES simulations looks slightly different due to only two grids being tested. The uncertainties are much larger, but the medium grid does not seem to be nearing mesh independence as with the RANS and URANS convergence test and neither grid tested with DES appears to predict C_L well.

The unsteady streamwise velocity along the rear slant shows that the coarser grid

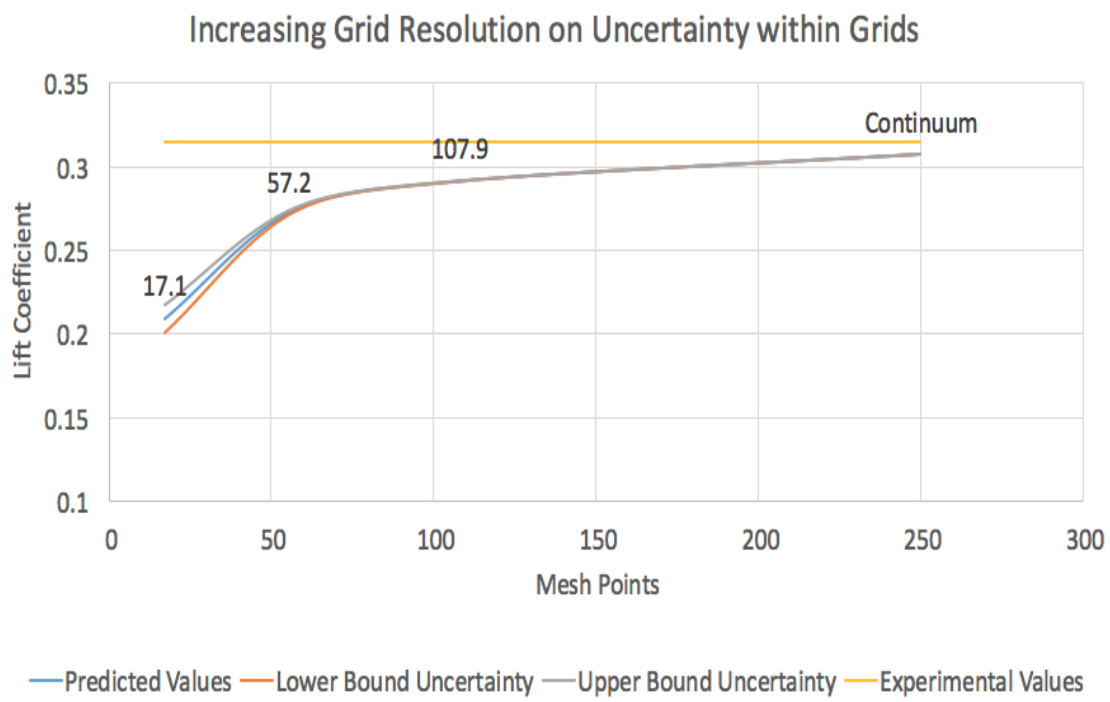

Figure 4.3: Graph of convergence as number of nodes increases to approximated continuum value for RANS C_L values

dissipates more of the minor fluctuations within the flow and is, therefore, not the best grid to perform unsteady simulations upon because minor characteristics of the flow will not be modelled due to the coarseness of the grid (Figure 4.7).

The vorticity plots show the clearest picture of what is happening as the grid is refined (Figures 4.8 and 4.9). As expected, flow features on the coarser grid get blurred and dissipated because there is not enough resolution to preserve the intricate flow features. Figure 4.8 fails to resolve the lengthwise vortices that form at the bottom of the body, which are present within Figure 4.9. The nature of the large C-pillar vortices is also different. The formation is very clear as in figure 4.9 as the flow rolls up onto itself as it travels down the rear slant, but this level of detail also gets dissipated in figure 4.8 even though the vortex core is still present. Small fluctuations seen in the more refined case are still seen in the coarse case, but their magnitude is much less due to the dissipation through the grid spacing.

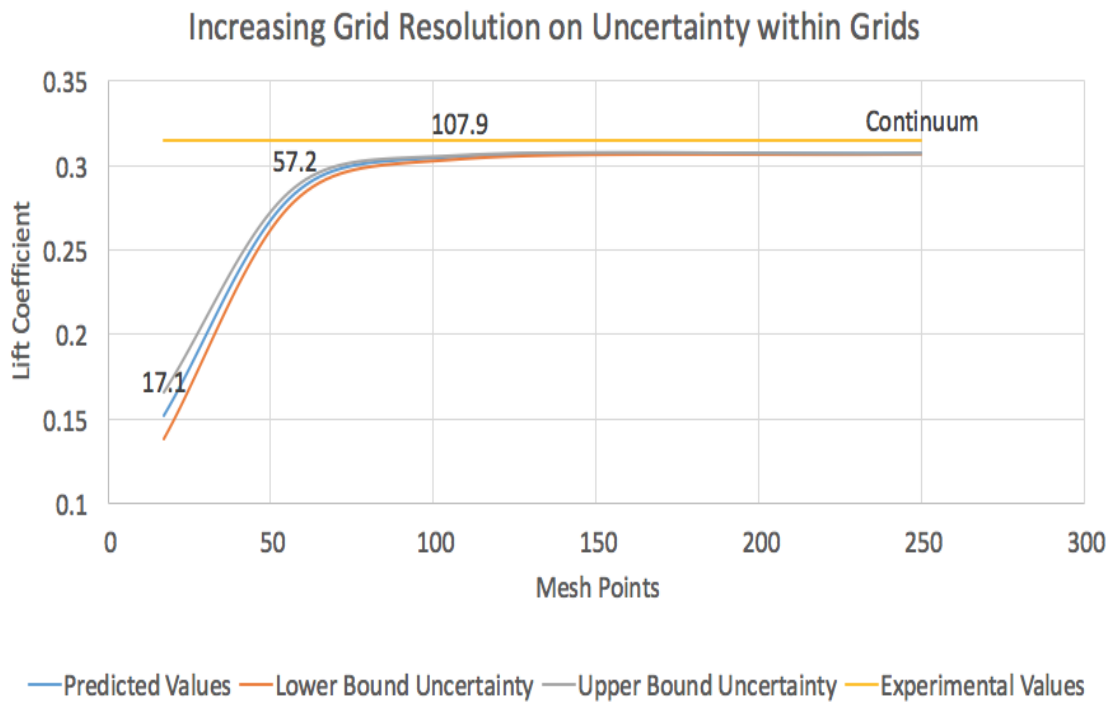

Figure 4.4: Graph of convergence as number of nodes increases to approximated continuum value for URANS C_L values

4.1.1 Time for Simulations to Run

The time taken for these simulations varied dramatically based upon their mesh size, number of cores per node, and solution method. The smallest simulation took 6 hours to run on 96 cores for the steady state RANS simulations, where the solution was completely converged after 5000 iterations. The medium sized simulation took $\approx$ 15 hours for a similar level of convergence after 5000 iterations on the same number of cores while the largest simulation took $\approx$ 30 hours on the same number of cores. The number of cores per node varied dramatically based upon computational use throughout the university. Ideally all simulations would have been node contiguous, which would have provided the fastest simulation times.

Unsteady simulations provided much longer simulation times. While steady state simulations relied upon number of iterations, the unsteady simulations relied upon

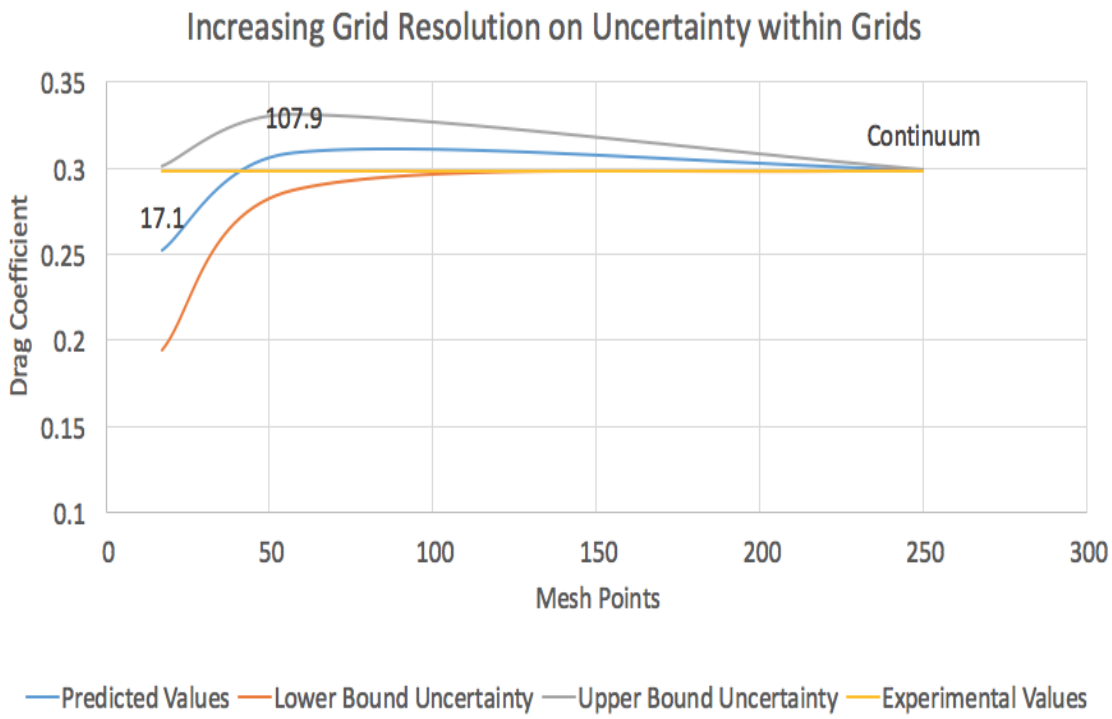

Figure 4.5: Graph of convergence as number of nodes increases to approximated continuum value for DES C_D values

the time step and an adequate time for the solution to converge. As stated above the simulations were run for 0.1 seconds all at a time step of 4.1667 x 10^{-6} seconds with a CFL number of 4 in order to speed up convergence. This small time step required 24,000 time steps in order to complete a simulation, each of which had 15 Newton subiterations. None of these simulations were node contiguous and subsequently took much longer to complete. Differences between simulation times are not significant, but DES simulations ran faster than URANS simulations due to the fact that DES simulations do not solve the equations of the turbulence model away from the wall. The basic grid refinements meant that 65% of the grid points were within the range of using the RANS equations, which meant that using DES was a very small time savings. The smallest simulation took 103 hours to complete the required number of time steps for a URANS simulation and 92 hours to complete a DES simulation. The medium simulation took $\approx$ 350 hours for the URANS simulation and 345 hours for

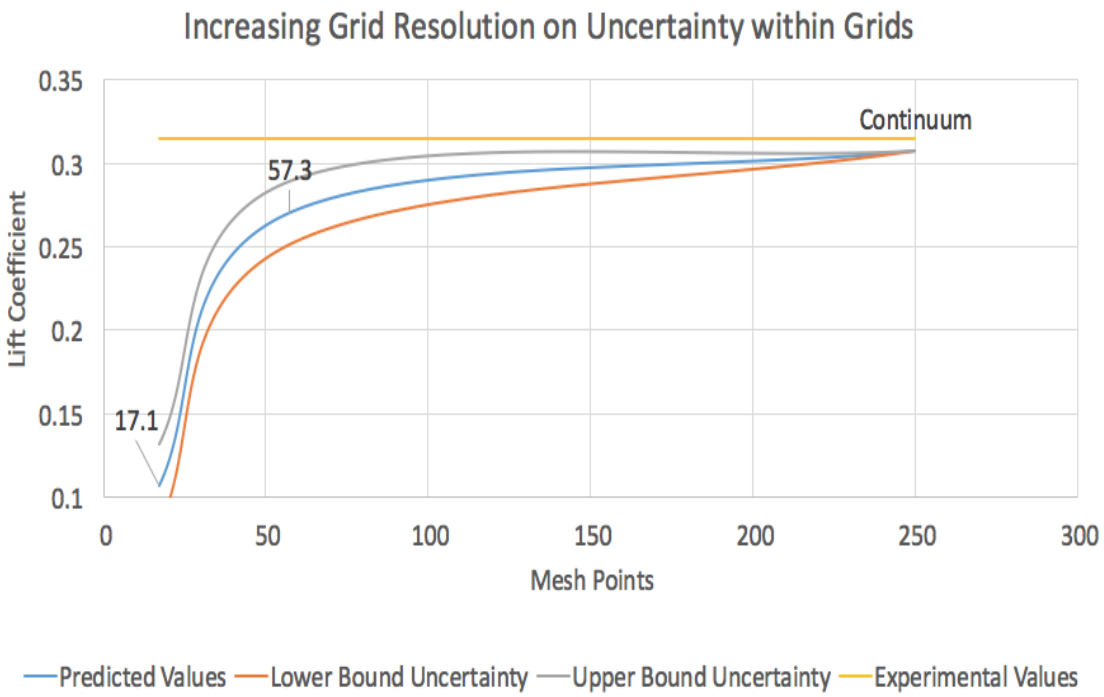

Figure 4.6: Graph of convergence as number of nodes increases to approximated continuum value for DES C_L values

the DES simulation, while the largest simulation took nearly twice as long requiring over 600 hours for the URANS simulation. All simulations used 96 cores with at least 4 cores per node.

4.2 Changing Rear Slant Angle

Using the optimal grid size, additional experiments test the ability of OVERFLOW and the grid to predict the forces upon the generic car model due to rear slant angle changes. Due to its varied flow structure, two sub-critical angles ($\phi = 20°$ and $25°$), the critical angle ($\phi = 30°$), and super-critical angle ($\phi = 35°$) are tested. Changes to the geometry were done only in CGT and the surface and volume mesh characteristics remained consistent with the baseline creation in order to reduce the number of changes to the mesh and ultimately all parameters altered. Each rear slant angle was simulated with both steady and unsteady RANS equations using the Menter SST

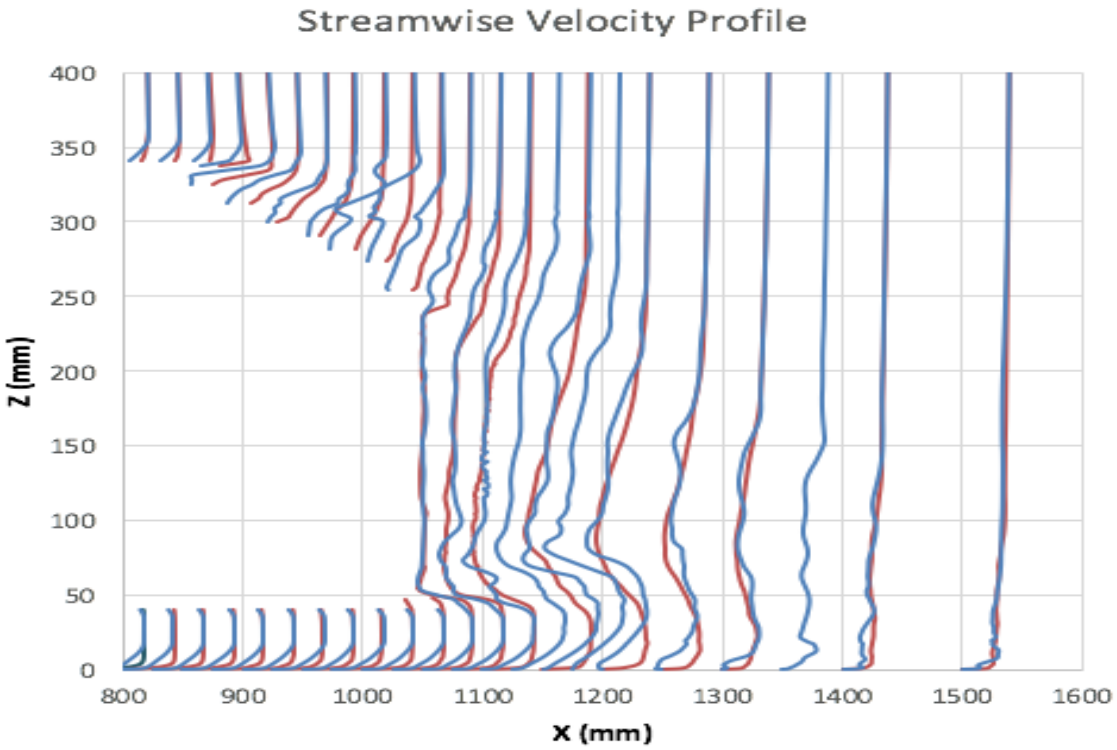

Figure 4.7: Unsteady Streamwise velocity at different grid densities. Orange lines show the streamwise profile of the coarsest grid (17.06 x 10^6 nodes) and Blue lines show the streamwise profile of the medium sized grid (57.2 x 10^6)

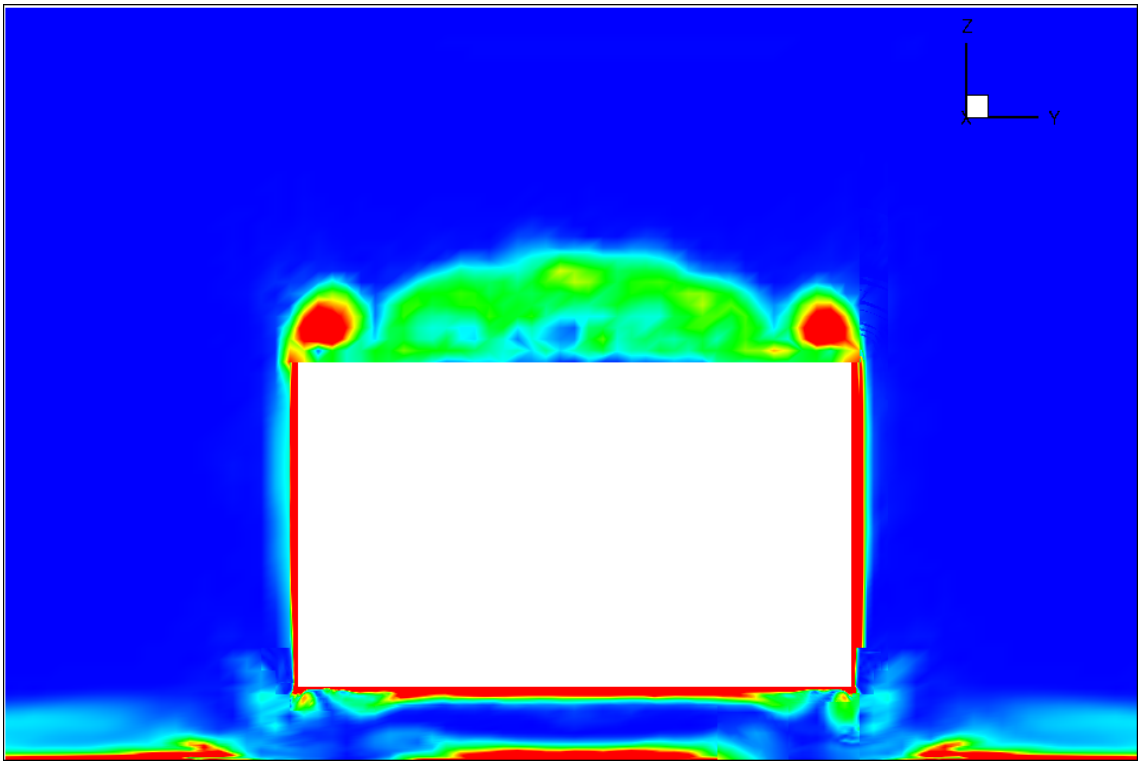

Figure 4.8: Vorticity magnitude at x = 1000 of coarsest mesh. Note differences between Figure 4.9, how the vortexes are smoothed and what features are dissipated

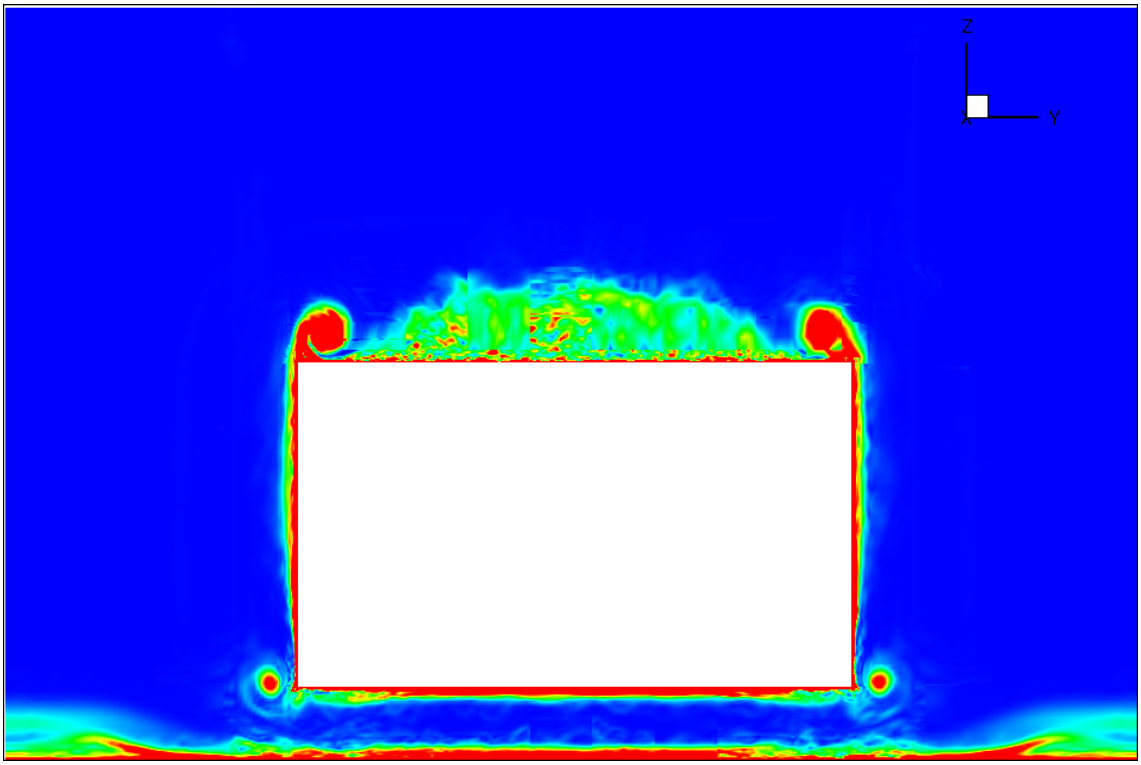

Figure 4.9: Vorticity Magnitude at x = 1000 for medium grid

Rear Angle	20	25	30	35
Experiment [2]	0.254 ±0.001	0.298 ±0.001	0.260 ±0.001	0.255 ±0.001
RANS	0.294 ±0.001	0.302 ±0.001	0.271 ±0.001	0.270 ±0.001
URANS	0.282 ±0.0042	0.302 ±.0045	0.279 ±0.0042	0.262 ±0.0039

Table 4.4: Comparison of C_D over various slant angles and experimental data[2]. Uncertainties were used from GCI results

Rear Angle	20	25	30	35
Experiment [7]	0.225 ±0.001	0.315 ±0.001	0.000 ±0.001	-0.050 ±0.001
RANS	0.167 ±0.0006	0.274 ±0.001	-0.089 ±0.0003	-0.050 ±0.0002
URANS	0.209 ±0.003	0.283 ±.0043	0.109 ±0.002	-0.056 ±0.0008

Table 4.5: Comparison of C_L over various slant angles and experimental data[7]. Uncertainties were used from GCI results

turbulence model.

4.2.1 Time Averaged Analysis

Reported in Tables 4.4 and 4.5, the drag forces are consistently over predicted by CFD. The only angle where the drag forces are predicted by CFD within experimental error is at the sub-critical angle of $\phi = 25°$. Coincidentally, the RANS and URANS predicted coefficients for drag was the exact same value and resulted in only being 1.3% from experimental measurements. Further from the critical angle, the predictions for $\phi = 20°$ are over-predicted by more than 10%. At higher angles the force coefficient is predicted much closer to the experimental data.

Looking only at the trends of the force coefficients, there is a definitive increase in drag as ϕ approaches the critical angle and a dramatic drop past the critical angle. For these data points, the trend is consistent with what is seen in the wind tunnel. The only exception between the experiment and CFD is that the flow was completely separated from the rear slant at the critical angle instead of being forced to separate by placing the splitter along the symmetry plane in the experiment. This suggests that the bifurcation of the flow, as shown in subsequent experiments, does not occur within the CFD simulations at the critical angle[57]. In both the RANS and URANS

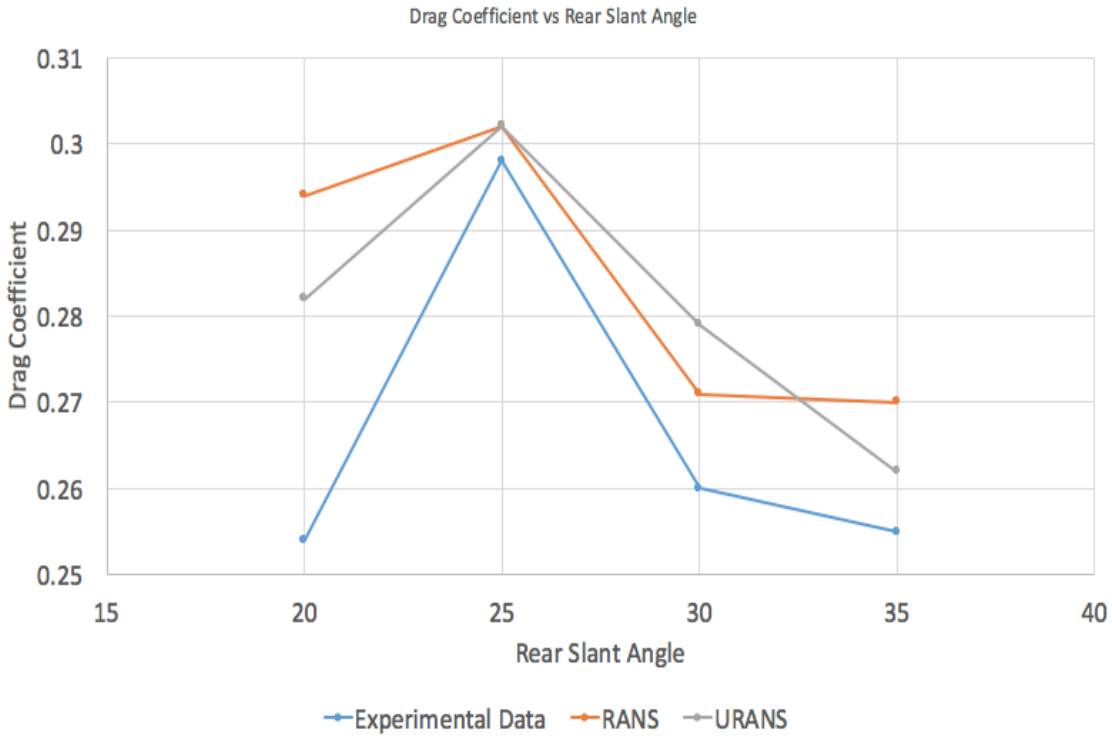

Figure 4.10: C_D plotted as a function of ϕ and compared to experimental data [2]

simulations the flow tended towards separating from the rear slant.

The lift coefficients, like C_D, had the same global trends as the experimental data and similar discrepancies between the magnitudes of the coefficients. Again the 20° angle was over predicted by a large margin, especially with the steady state simulation where C_L was under-predicted by over 25%. Reflected in C_D, the high levels of lift predicted at the critical angle is not seen within the simulations as the flow separates, but CFD also does not predict a neutral vehicle. The steady state simulation predicts 89 counts of downforce, while the unsteady simulation predicts 109 counts of lift, neither of which is close to a neutral lift value. At the super-critical angle, the lift predictions are very close in absolute magnitude, but do not have overlapping levels of uncertainty.

The λ-2 criterion, which highlights vortex cores, shows an excellent view of the flow field. As the rear slant increases, the speed of the flow over the rear slant increases

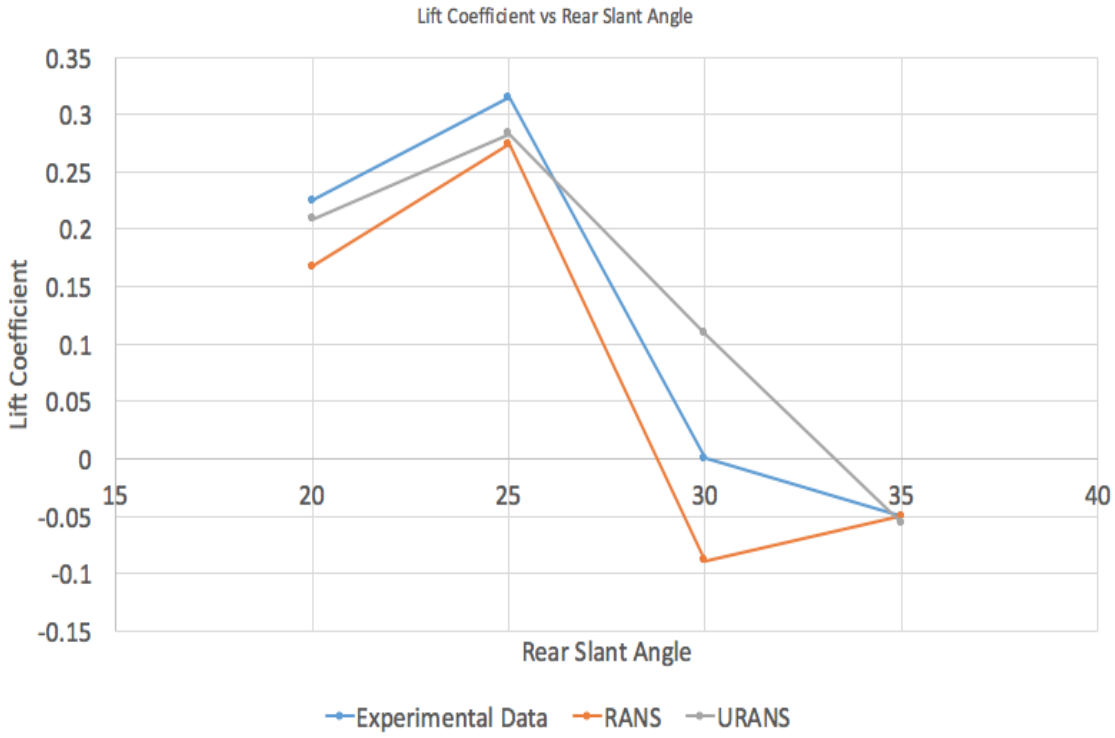

Figure 4.11: C_L plotted as a function of ϕ and compared to experimental data

and the c-pillar vortices increase in size. At and beyond the critical angle, the c-pillar vortices are indistinguishable from the separated flow along the rear slant. The longitudinal vortices, flow separation at the front of the body, and horseshoe vortices along the body are all present at all angles.

Looking at the flow field in figures 4.16 and 4.17, the simulations compare well to experimental data for the 25° rear slant angle, the URANS simulations predict a streamwise velocity similar to other CFD simulations (Figures 4.16 and 4.17), but ultimately predict a closer C_D value including those that use hybrid RANS/LES methods (Table 4.6). The main apparent difference between the other CFD simulations and the ones depicted above is the difference in the number of nodes or volumes used to discretize the computational domain. While the other simulations use different turbulence models, the grid size is two to four times smaller than the simulations within this thesis with the largest size used in the simulations by Serre *et.al* [48][5][32]. Even

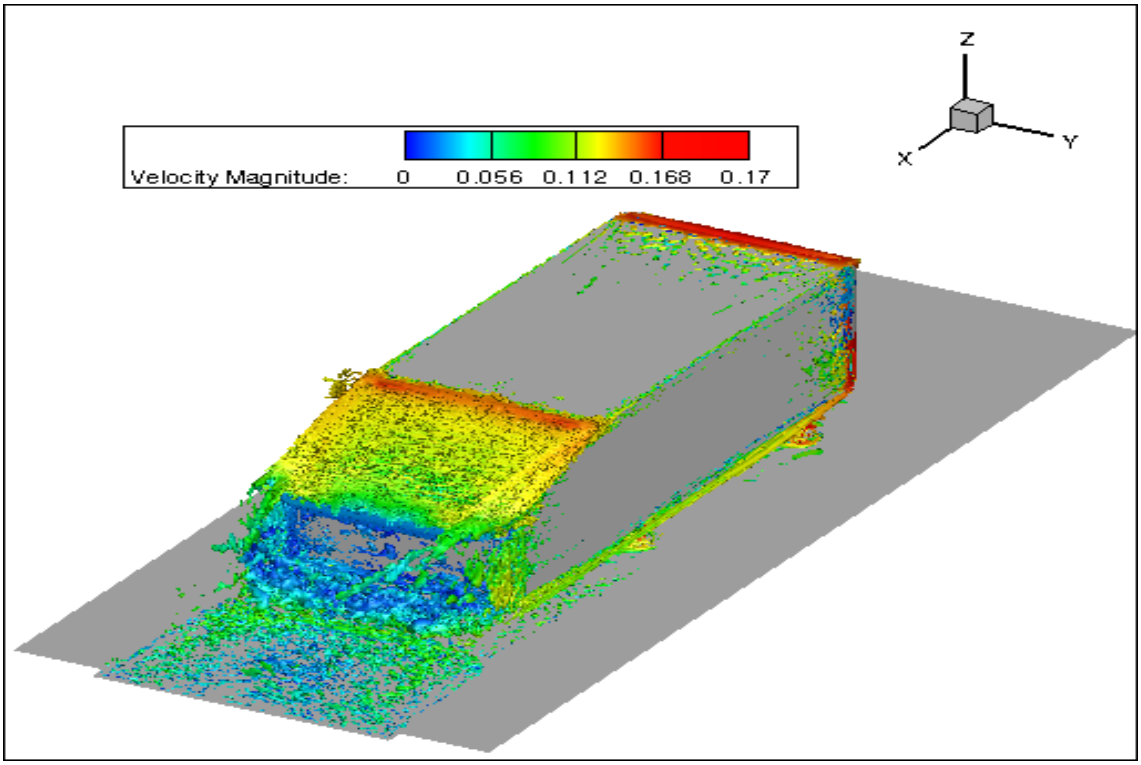

Figure 4.12: $\lambda - 2$ Criterion at -1 x 10^{-6} of $\phi = 20°$ colored by velocity magnitude

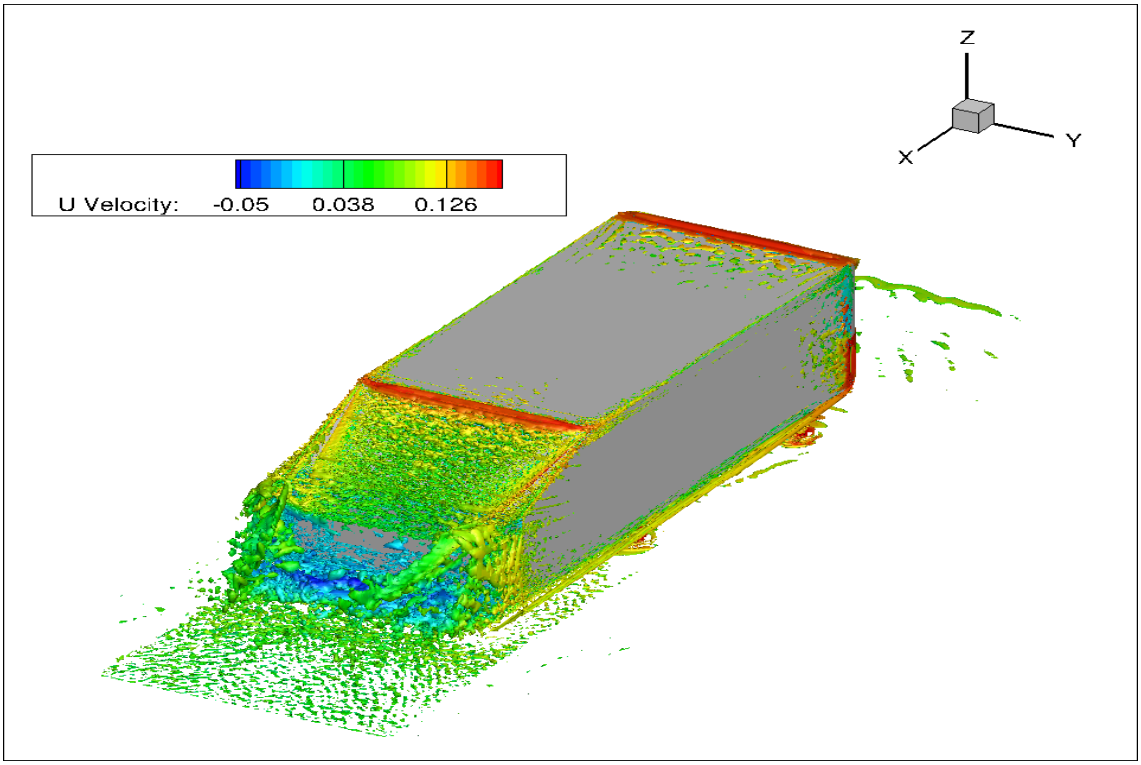

Figure 4.13: $\lambda - 2$ Criterion at -1x10^{-6} of $\phi = 25°$ colored by streamwise velocity

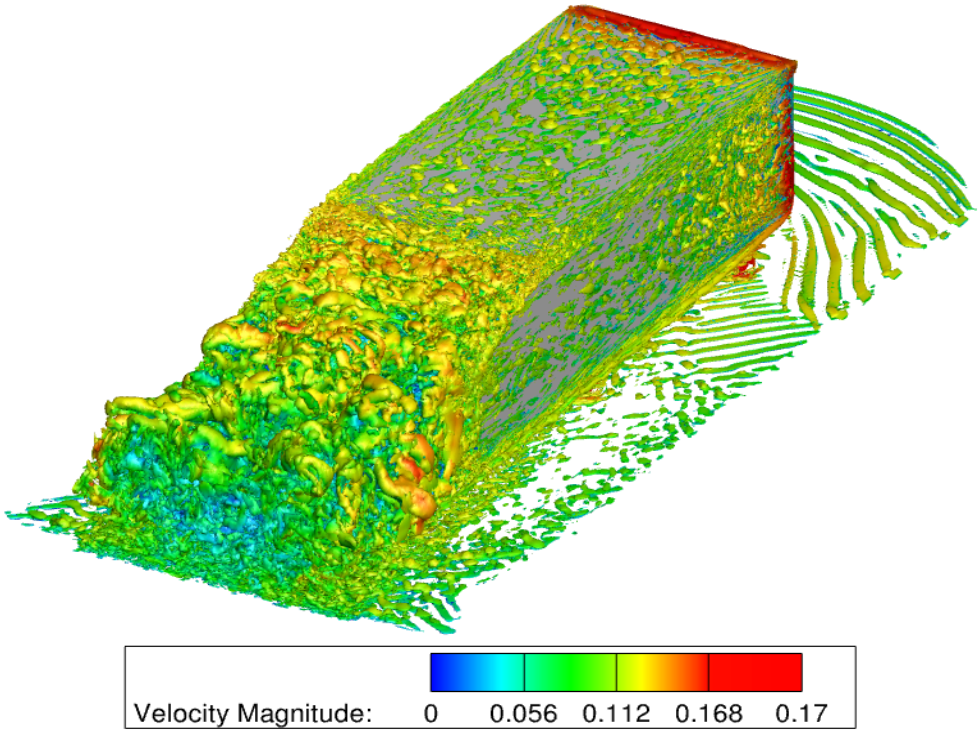

Figure 4.14: Unsteady $\lambda - 2$ Criterion at -1 x 10^{-6} of $\phi = 30°$ colored by streamwise velocity

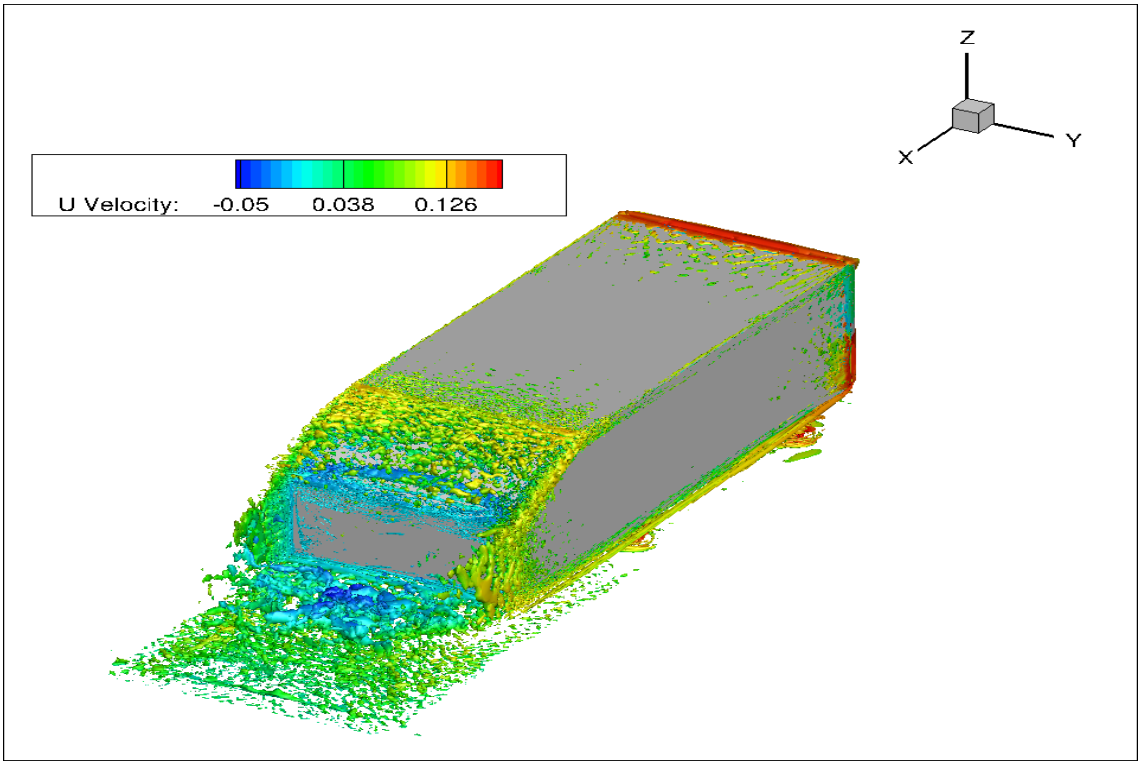

Figure 4.15: $\lambda - 2$ Criterion at -1 x 10^{-6} of $\phi = 35°$ colored by streamwise velocity

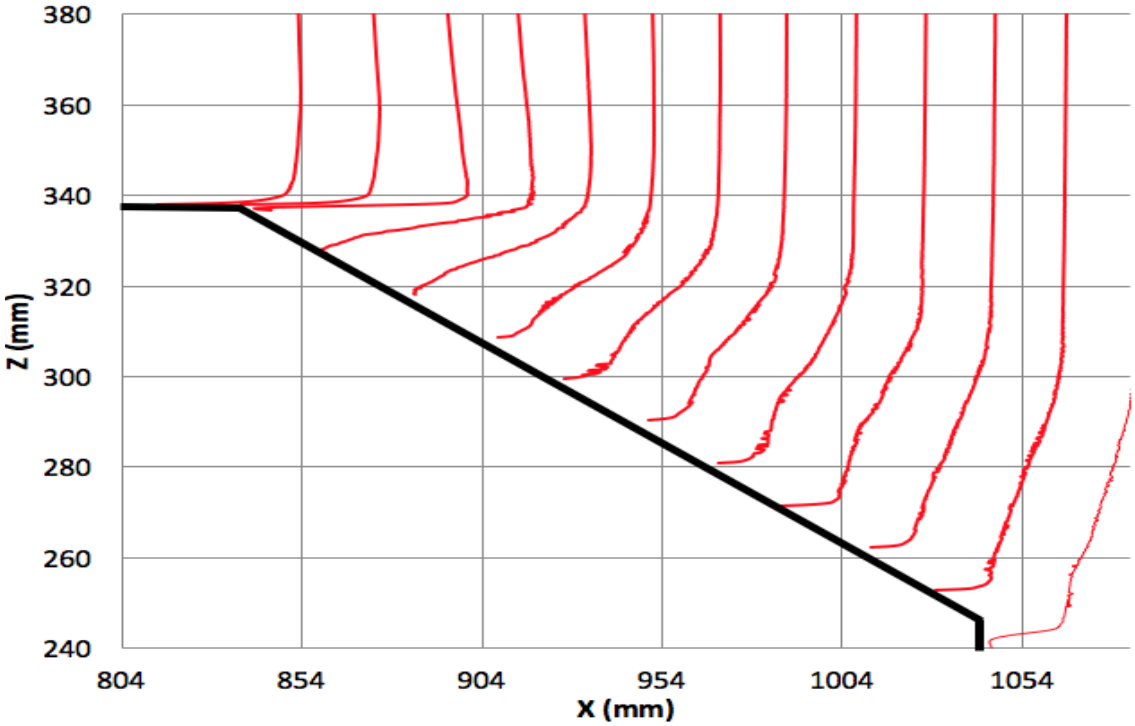

Figure 4.16: Streamwise velocity profile of URANS simulation at $\phi = 25°$

though the rear slant angles were tested only with steady and unsteady RANS, the smaller scales were able to be resolved with more refined grids that results in the increased accuracy seen in comparison to the other simulations.

The one main difference between the experimental results and those acquired through the URANS simulations is that the velocity near the wall increases rapidly when predicted by CFD. Off the wall the slopes are extremely similar, but in the 10 mm region before they become more similar, the velocity profile of the CFD simulation looks more akin to the growth of the flat plate boundary layer.

CFD simulations conducted by Menter [34] testing different turbulence models with steady and unsteady simulations used 1st and 2nd order finite-volume methods. Depending on the order of accuracy the flow would either stay attached to the rear slant (1st order) or separate (2nd order). Neither of these two simulations agree with the streamwise velocity profiles of experimental data or the data from the above

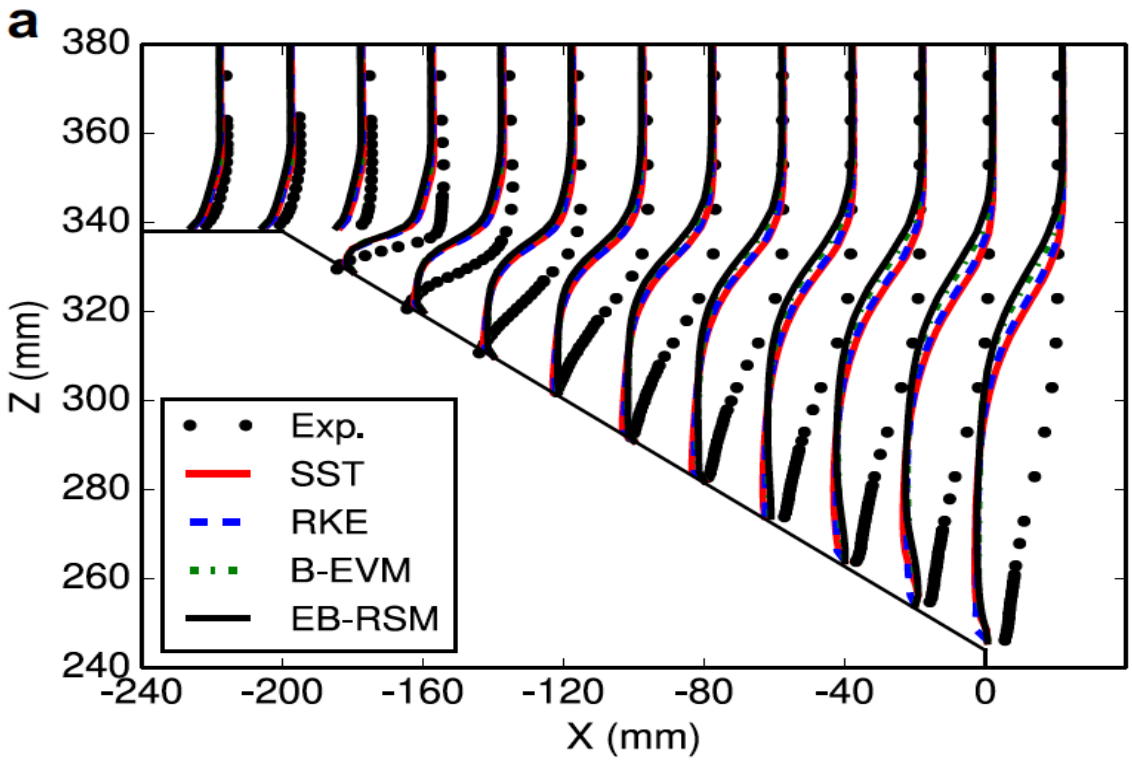

Figure 4.17: Streamwise velocity profile of rear slant at $\phi = 25°$; turbulence model data from[4], experimental data from [2]

Reference	Reynolds Number (10^6)	Mesh Count (10^6)	Solver-Type	C_D
Serre *et. al.* [48]	0.768	23	DES-SST	0.343
Serre *et. al.* [48]	0.768	40	LES-NWR	0.346
Serre *et. al.* [48]	0.768	18.5	LES-NWM	0.317
Serre *et. al.* [48]	0.768	21.3	LES-SW	0.431
Bayraktar [8]	1.2	10	RANS	0.288
Meile [32]	1.2	5	RANS	0.288

Table 4.6: Comparison of C_D at 25° with other CFD simulations

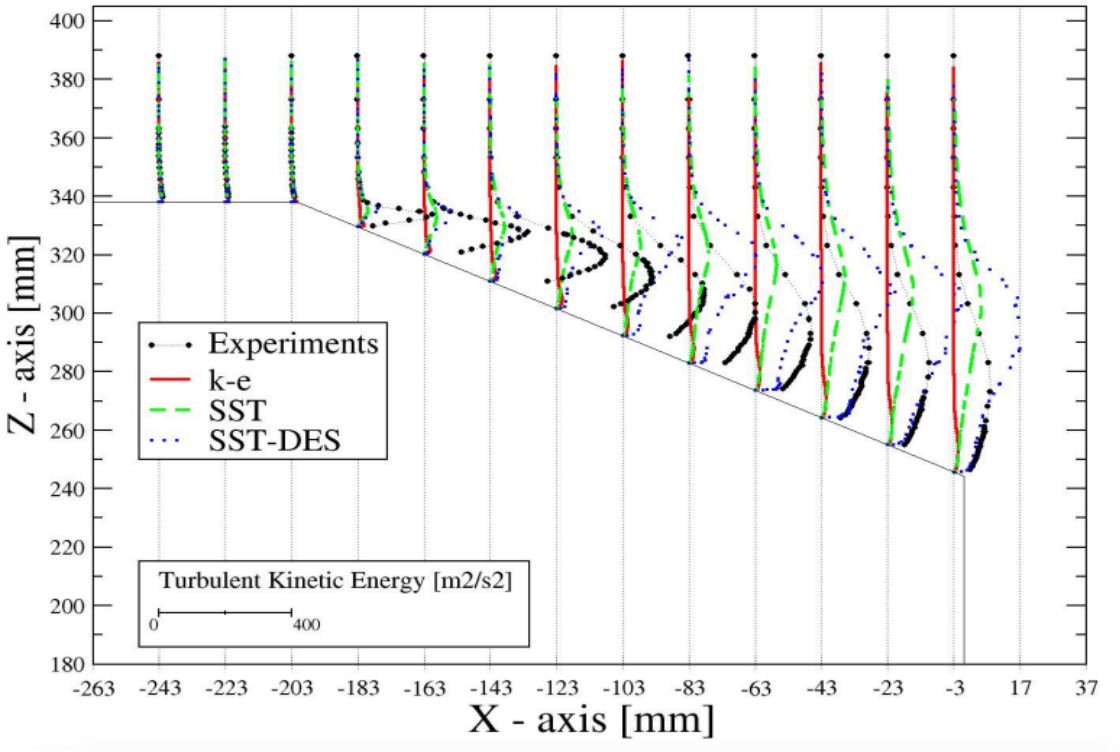

Figure 4.18: Turbulent Kinetic Energy along symmetry plane $\phi = 25°$[35]

simulations (Figure 4.18) [62][35]. While Menter did not report force coefficients, solely by looking at the streamwise velocity profiles, it was concluded that the forces were not in agreement with data received [35]. Improvements in predicting drag forces came from LES and DES simulations of Serre *et. al.*[48], but the simulations were coarser than those within this current study . The closest prediction to experimental values was the LES-NWM simulation with three times less grid points (Table 4.6). Each of the simulations predicted a higher level of turbulent kinetic energy than those of [34], but the coarseness of the simulations reduced its ability to predict the same levels of turbulent kinetic energy as in experimental data and in the simulations (Figure 4.19[48]).

The separation at the critical angle can be attributed to modelling errors within the SST turbulence model. While most experiments and simulations discussed did not test the critical angle, symmetry plane slice of TKE appears very different between

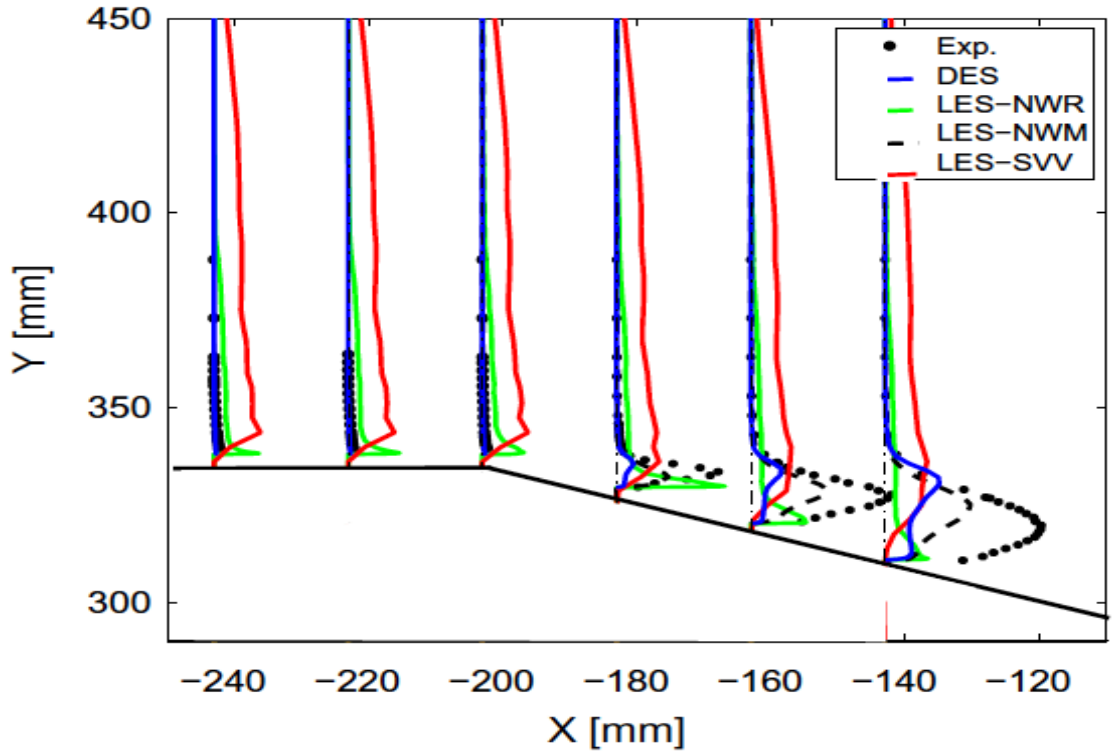

Figure 4.19: Turbulent Kinetic Energy along symmetry plane $\phi = 25°$[48]

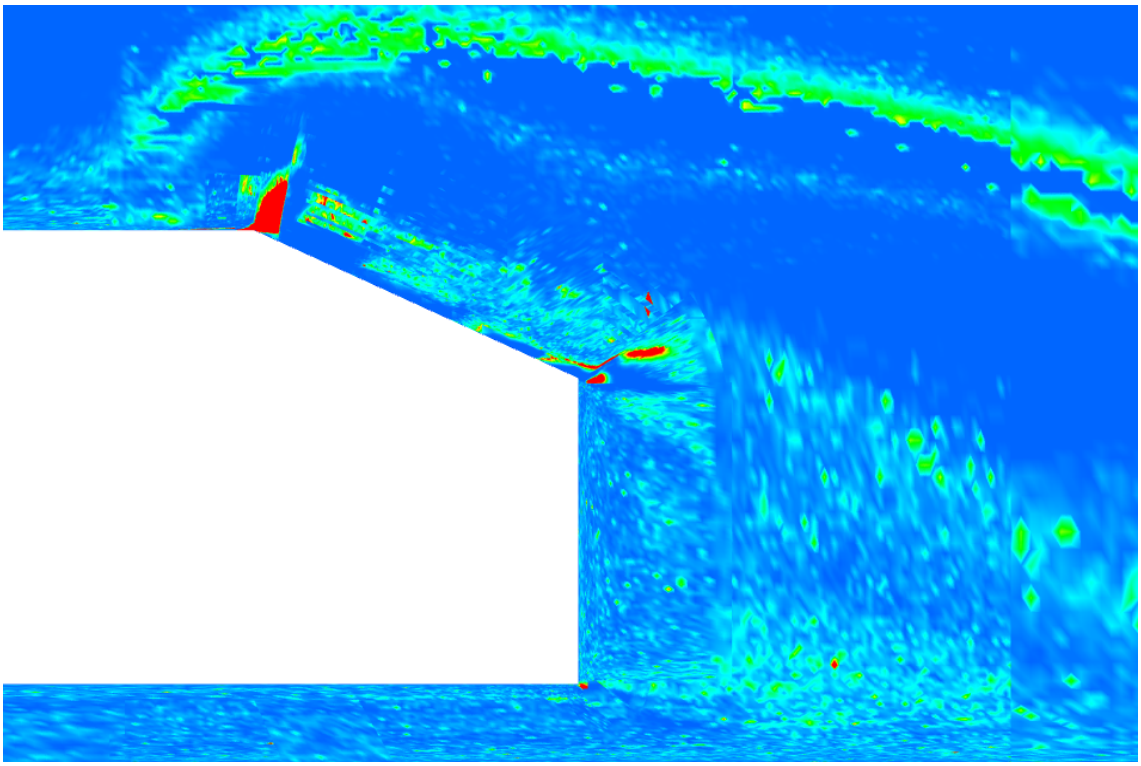

Figure 4.20: Turbulent Kinetic Energy at the sub-critical angle. Red indicates where the TKE limiter is active.

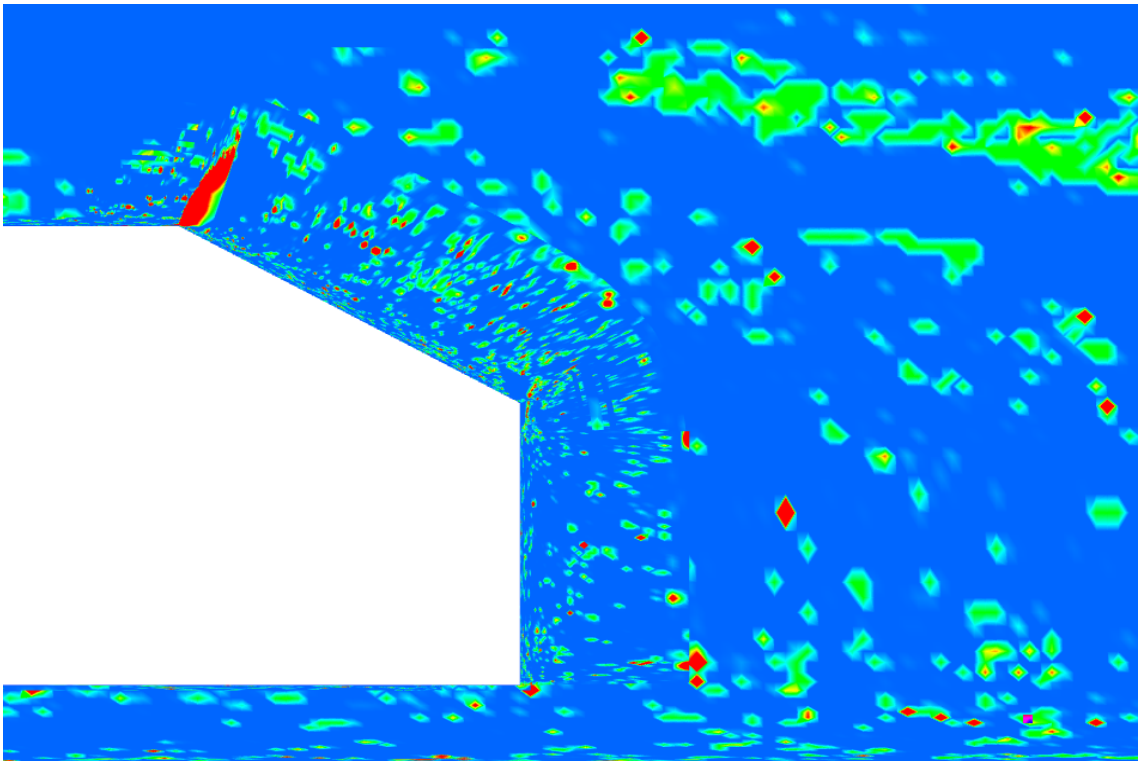

Figure 4.21: Turbulent Kinetic Energy at the critical angle. Red indicates where the TKE limiter is active.

the critical and sub-critical angles. While a skin friction (C_f) plot would increase the ability to make conclusions in this region, the characteristics of the baseline SST model help explain why it is separating at the critical angle. The baseline SST model limits the production of turbulent kinetic energy near the wall to keep it proportional to shear-stress within this region through the blending function ($F2$ in equation (3.20))[15]. The increase in turbulent kinetic energy as the rear slant angle increase allows the flow to stay attached or reattach further down the model. At the critical angle, and possibly before $\phi = 30°$, the turbulent kinetic energy is limited at the sharp corner and therefore does not have the ability to energize the boundary layer and either stay attached or reattach further down the model. This limiting characteristic within the SST model, a product of model coefficients calibrated for certain flow phenomena, violates energy conservation within this particular region of the flow. This phenomenon can be avoided and should be tested by adjusting the a_1 coefficient,

which can increase the eddy viscosity and reduce the limiting effect of the SST model [15].

4.2.2 Unsteady Analysis

For unsteady analysis of vortex shedding, the main value to report is the non-dimensional Strouhal number, which describes the relationship between the frequency of vortex f and ratio of characteristic length and bulk flow velocity ($\frac{L}{U}$) as shown below (4.22).

$$St = \frac{fL}{U} \tag{4.9}$$

The prevalence of more unsteady flow data non-simple geometric shapes is gaining popularity due to studies on active flow control. Studying these structures and comparing them to experimental and numerical data means looking at the Strouhal numbers of circular and square cavities. In two dimensions these shapes have analytical solutions relating their Reynolds number (Re), drag coefficient (C_D), and Strouhal number (St) and can be extended into three dimensions with some corrections to these relationships [1]. These results have been applied to other geometric shapes and bluff bodes since a characteristic feature of the vortex street produced within the wake is its general geometric similarity regardless of the bluff body that generated it [44]. This phenomenon made Roshko postulate about a 'universal' Strouhal number based upon the width of the wake [44]. A universal Strouhal number is reasonable within a range of Reynolds numbers from the onset of turbulence within a flow to the drag crisis region, approximately Re = 1000 to 10^5 (Figures 4.22 and 4.23). Within this region of Reynolds numbers, the drag of a cylinder gradually decreased until near Re = 10^6 where it drops off dramatically and the Strouhal number increases considerably. Without the drag crisis region, a universal Strouhal number may have been true within a range of values. All further simulations are within this high Reynolds value

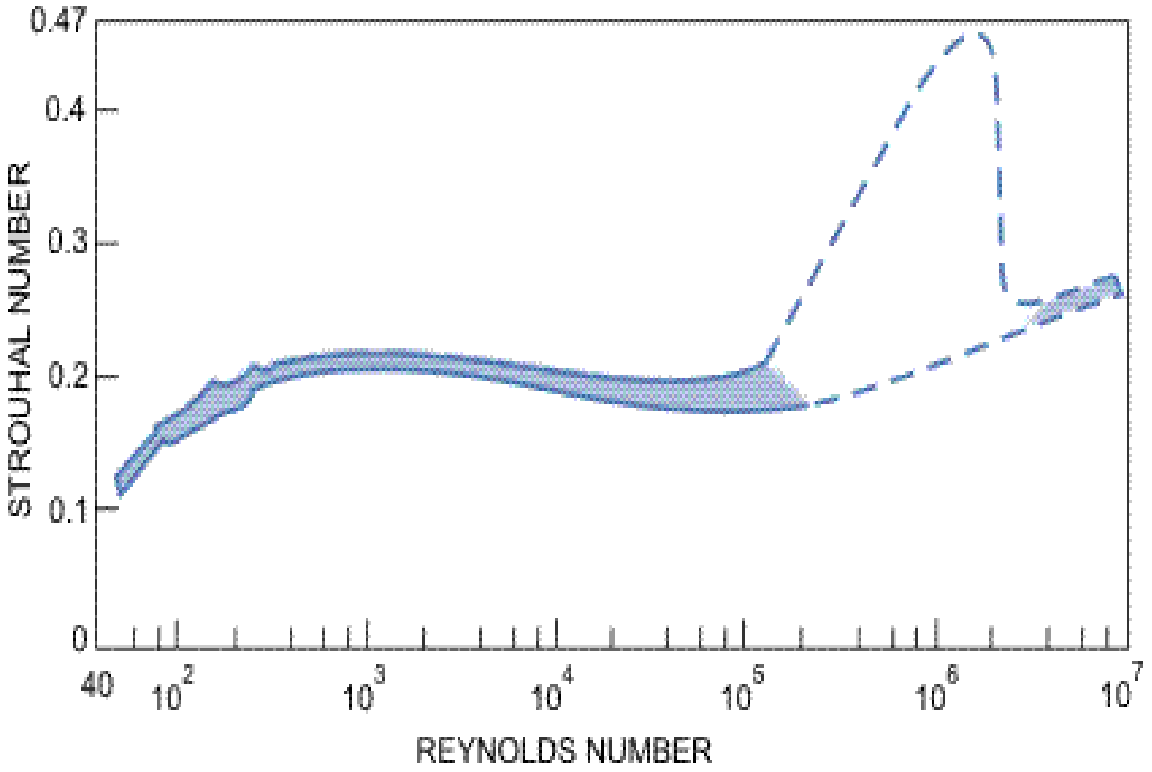

Figure 4.22: Relationship between Strouhal number and Reynolds number [10]

region, which is in the region of drag crisis for a circular cylinder.

Each of the equations below is some approximated relationship between either Strouhal number and Reynolds number or Strouhal number and C_D based upon the flow of a cylinder. These equations were derived geometrically by the size of the wake (Equation (4.10)[1]), extrapolation from a frequency relationship of a laminar wake (Equation (4.11)[44]), or by an energy relationship caused by a relationship between C_D and and vortex shedding (Equation (4.12)[45]).

$$St = \frac{1}{2^{3/4}\pi}\sqrt{C_D + 1} \tag{4.10}$$

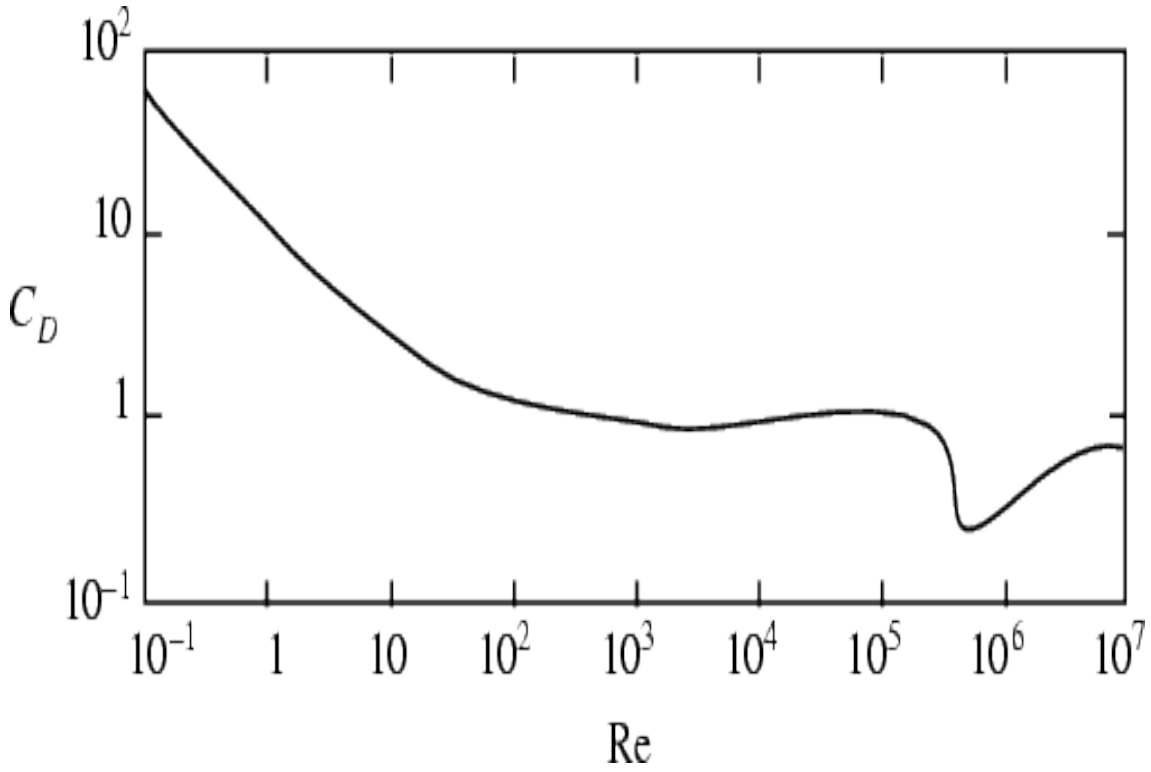

Figure 4.23: Relationship between C_D and Reynolds number [55]

$$St = 0.212\left(1 - \frac{21.2}{Re}\right) \tag{4.11}$$

$$ST = 0.077\left(\frac{C_D + 1}{C_D}\right) \tag{4.12}$$

Multiple studies have been performed on generic simplified car models in order to understand the 3D flow structures [2][62][38]. Subsequent studies have confirmed

Table 4.7: Comparisons of Frequency and Strouhal number of vortex shedding on the rear slant from varied rear slant angles. Reynolds number is based upon height

Rear Slant Angle	Reynolds Number (10^5)	Frequency (Hz)	Strouhal Number
Experiment at 25°[13]	7.68	39.75 Hz	0.199
Experiment at 25°[61]	0.502	14.6 Hz	0.196
Experiment at 25°[54]	7.68	23.9 Hz	0.2
20	7.68	22.3 Hz	0.187
25	7.68	25.5 Hz	0.213
30	7.68	28.7 Hz	0.240
35	7.68	29.2 Hz	0.244

these initial results on multiple different automotive shapes, but these have all been predominately focused around time averaged flow structures. Since these studies have opened the door on the flow structures evident on most vehicles, the intricate unsteady mechanisms, while noted are not intensively reported. Active control over these structures are of interest to the automotive industry due to the potential to further reduce the drag on vehicles as well as in the motorsports industry, which is focused on extracting incremental elements of performance for an overall gain across the car.

Recent experiments have looked at the shedding of the separated and toric structures behind the Ahmed body mainly at the sub-critical 25° angle case due to the increased complexity of the separation and reattachment along the rear slant. At the sub-critical angle of $\phi = 25°$, Strouhal numbers have previously been reported with a varying range from 0.18 to 0.5 over the rear slant to 0.36 to 0.53 in the wake of the body[61].

The CFD simulation predicted Strouhal numbers from a point directly behind the rear slant corner (15 mm) to measure the separation off the top of the model, and a point $0.25L$ behind the model along the symmetry plane. These do not correlate exactly to the experimental points of measurement, but capture similar flow features.

The Strouhal number off of the rear slant was compared to simple two dimensional ramp experiments. The experimental data was tested at a Reynolds number an order

Table 4.8: Comparisons of Frequency and Strouhal number of vortex shedding in the rear wake from varied rear slant angles at $0.25L$ from the end of the model

Rear Slant Angle	Frequency (Hz)	St
20	38.7 Hz	0.324
25	40.2 Hz	0.336
30	39.6 Hz	0.331
35	41.5 Hz	0.347

of magnitude lower than the simulations (Re = 1.3 x 10^5 compared to 0.768 x 10^6)[13]. The simulation data predicted vortex shedding at a slightly higher Strouhal number than those of the three dimensional experimental data. When compared to the trends of Strouhal number vs Reynolds number of a cylinder, this increase should be expected since it is assumed that the vortex shedding of the Ahmed body is not independent of Reynolds number. Likewise, the comparisons between the results of Debien and Zheng are similar due to both experiments using roughly the same Reynolds number [13][61]. The interesting development is the results presented by Thacker, which were run at the same Reynolds number as the current simulations, but still received the same Strouhal number on the rear slant as previous experiments [54].

The Strouhal numbers predicted within the rear wake when compared to Zheng's experiment are not similar since the experimental values are all more than 20% smaller [61]. Within the simulation the extra dissipation due to the SST model over-damping the vortices can be a result of these results as well as the failure to measure the simulation data at the exact same position as the experimental data. While the simulation data does not compare well to that of Zheng, it compares reasonably well to analytical solutions between the relationship of C_D and Strouhal number as in Equation (4.12).

While all of the calculated values within Table 4.9 are from relationships derived from experimental data around circular and square cylinders, the agreement is within 7.5% for all cases. This result suggests that approximating bluff bodies as circular cylinders to receive bulk magnitude vortex structures is a valid method. The result

Table 4.9: Comparisons of Frequency and Strouhal number of vortex shedding in the rear wake from varied rear slant angles at 0.25L from the end of the model

Rear Slant Angle	Frequency (Hz)	$St_{\sqrt{A}}$	Calculated St from Eq. (4.12)	% Error
20	38.7 Hz	0.324	0.350	7.4%
25	40.2 Hz	0.336	0.332	-1.2%
30	39.6 Hz	0.331	0.353	6.2%
35	41.5 Hz	0.347	0.371	6.5%

of tuning the simulation to the $\phi = 25°$ case still shows up in the calculated value for Strouhal number based upon Equation (4.12), since C_D was the variable used to calculate the resulting Strouhal number.

4.3 RANS vs URANS vs Hybrid RANS/LES methods

Changing the turbulence model did not have as significant of change to the forces on the model as changes to the rear slant angle since most of the predicted results are similar to each other. Compared to the simulations of other works, most notably the LES simulations of Serre *et. al*, the drag prediction is significantly closer [48]. Predictably the DES simulation over predicted the drag force and under predicted the lift force due to the increased turbulent kinetic energy created by the switch from RANS to LES modeling. This is rectified by using the DDES and Multi-Scale models, which predict values closer to the experimental measurements [2].

The streamwise velocity profiles mirror that predicted by the forces where the DES simulation varied more dramatically than the other four simulations (Figure 4.24) . Minor differences within the wake show that the DDES simulation predicts a higher speed recirculation zone and mirrors the URANS result above the recirculation zone. The Multi-Scale model and URANS simulations predict nearly the same velocities throughout the recirculation zone but diverge slightly above this region. As the flow traveled into the far field, the wake patterns disappeared and all of the simulations had nearly identical velocity profiles.

At this level of refinement, other than comparing directly to errors of experimental

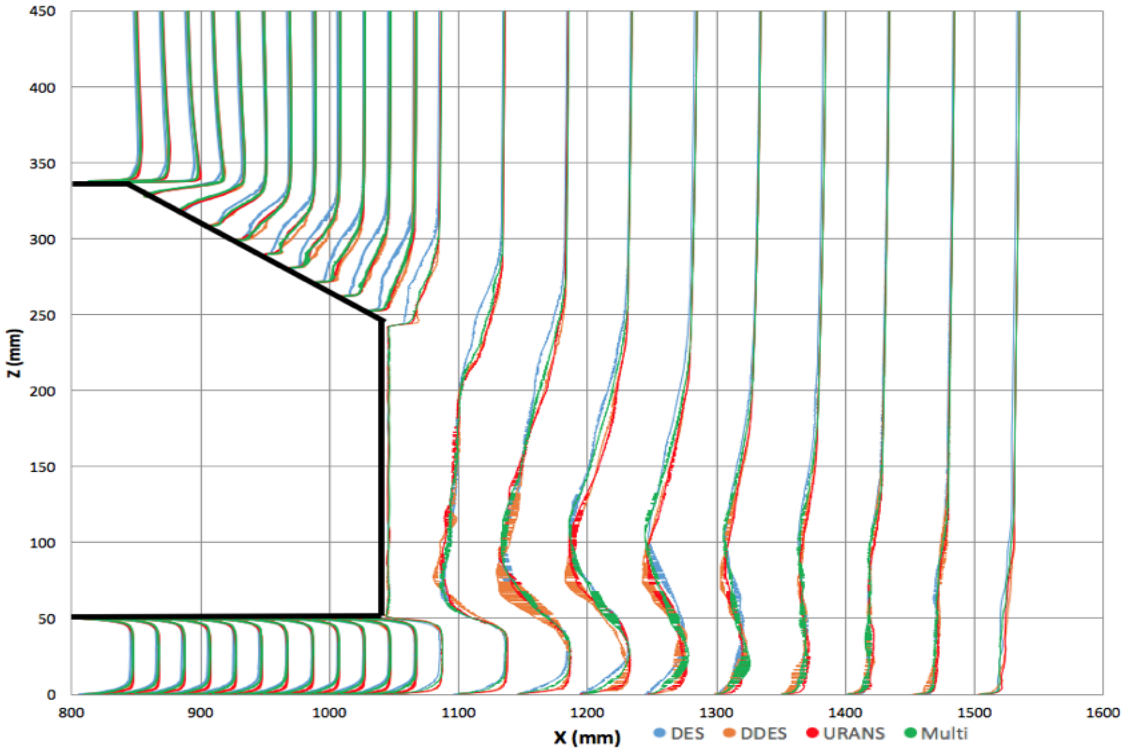

Figure 4.24: Streamwise velocity profile of unsteady simulations. URANS shown in Red, DES shown in Blue, DDES shown in Orange, and the Multi-Scale Model shown in Green

Solver	C_D	C_L	% Error from [2]	% Error from [7]
Experiment [2][7]	0.298 $\pm$0.001	0.315 $\pm$0.001	-	-
RANS	0.302 $\pm$0.001	0.274 $\pm$0.001	-1.3	13.0
URANS	0.302 $\pm$0.005	0.283 $\pm$0.001	-1.3	10.2
DES	0.309 $\pm$0.022	0.270 $\pm$0.019	-3.7	14.3
DDES	0.304 $\pm$0.021	0.282 $\pm$0.019	-1.7	10.5
Multi-Scale	0.304 $\pm$0.021	0.281 $\pm$0.019	-2.0	10.8

Table 4.10: Comparison between experimental results and various solvers

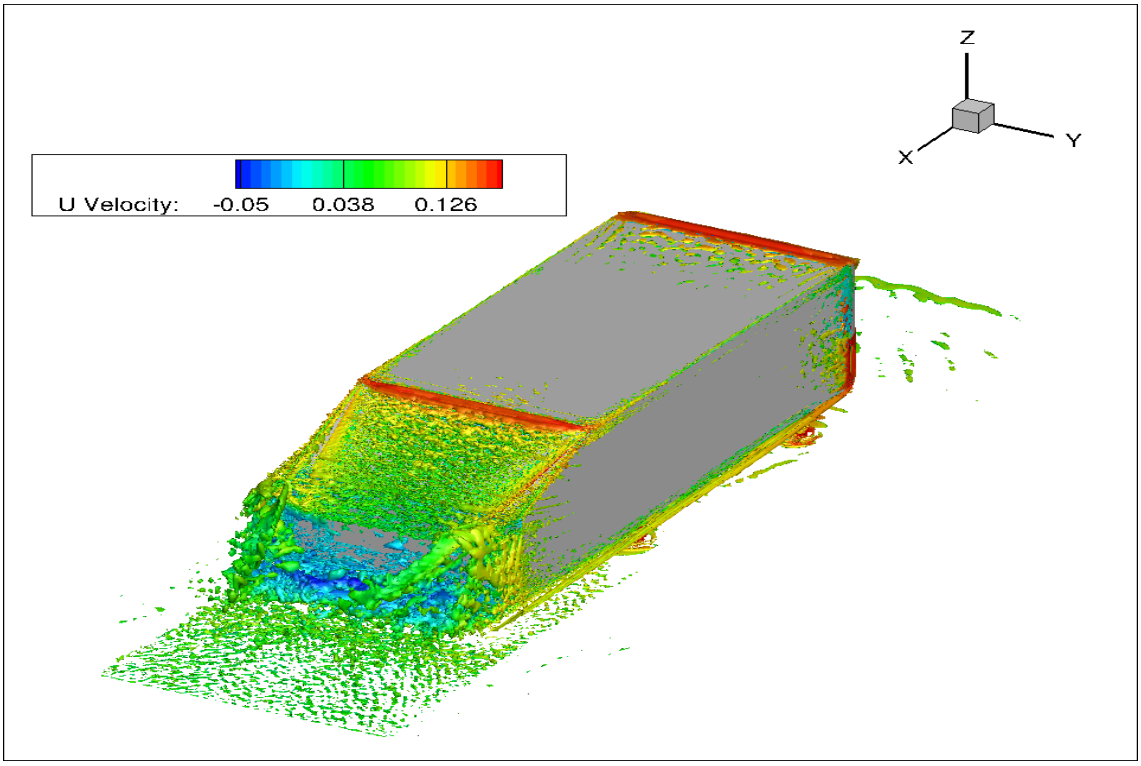

Figure 4.25: λ-2 Criterion at -1 x 10^{-6} for URANS simulation at $\phi = 25°$ colored by streamwise velocity

data, there is no significant difference between either method. The error as computed by the grid convergence study means that all of the errors overlap resulting in indistinguishable force results. Based upon only an increased prediction of C_L and marginally shorter run time (5 hours shorter), further studies of this magnitude should be done with the DDES model.

The unsteady results also reflect the indistinguishable force results. While they still do not agree with experimental data, each method predicts nearly the same Strouhal number for both the rear slant and rear wake.

4.4 Refined Comparison of Wake at Two Distinct Rear Slant Angles

Due to the inconclusive results of the previous study, the refinement of the mesh around the wake was extended a full body length behind the model and the SST-DDES model was used to simulate the sub-critical and super-critical angles with this

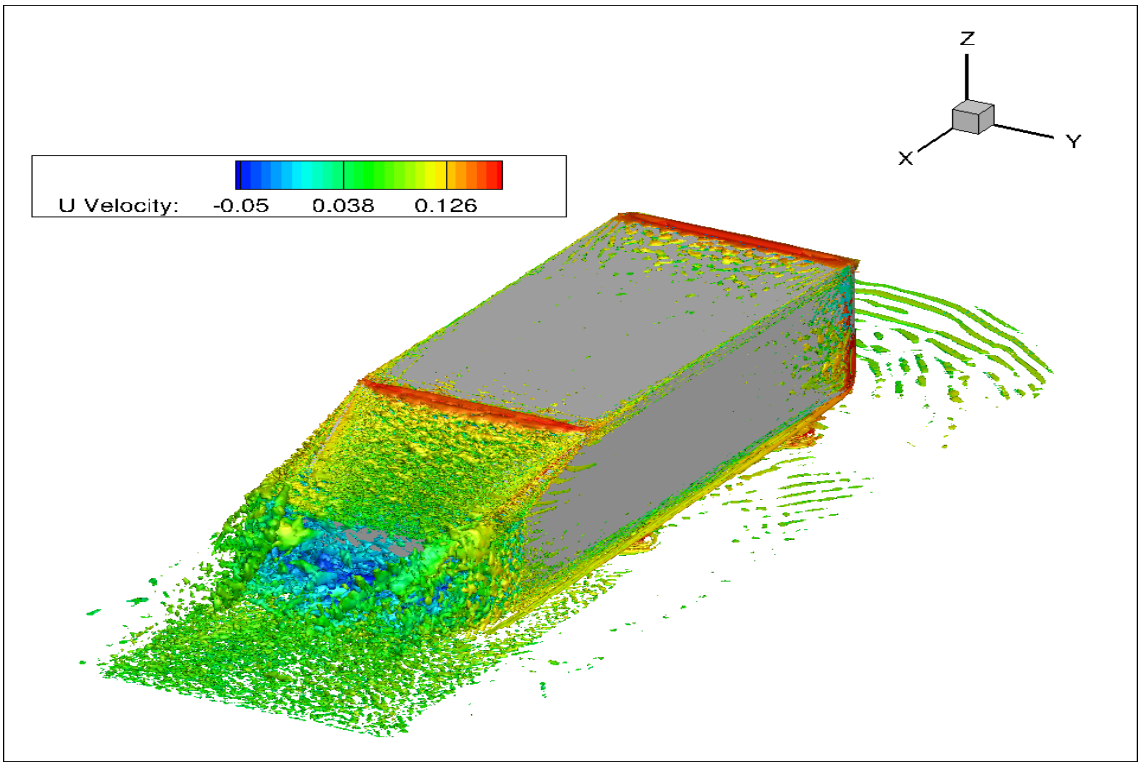

Figure 4.26: λ-2 Criterion at -1 x 10^{-6} for URANS simulation at $\phi = 25°$ colored by streamwise velocity

Table 4.11: Comparisons of Frequency and Strouhal number of vortex shedding on the rear slant with RANS and hybrid RANS/LES models

Solver	Frequency (Hz)	$St_{\sqrt{A}}$
Experiment [61]	14.109 Hz	0.196
URANS	25.5 Hz	0.213
DES	25.7 Hz	0.215
DDES	29.2 Hz	0.244
Multi-Scale	28.5 Hz	0.238

Table 4.12: Comparisons of Frequency and Strouhal number of vortex shedding on the rear slant with RANS and hybrid RANS/LES models

Solver	Frequency (Hz)	Strouhal
Experiment [61]	31.816 Hz	0.442
URANS	40.2 Hz	0.336
DES	35.4 Hz	0.296
DDES	38.9 Hz	0.326
Multi-Scale	42.1 Hz	0.352

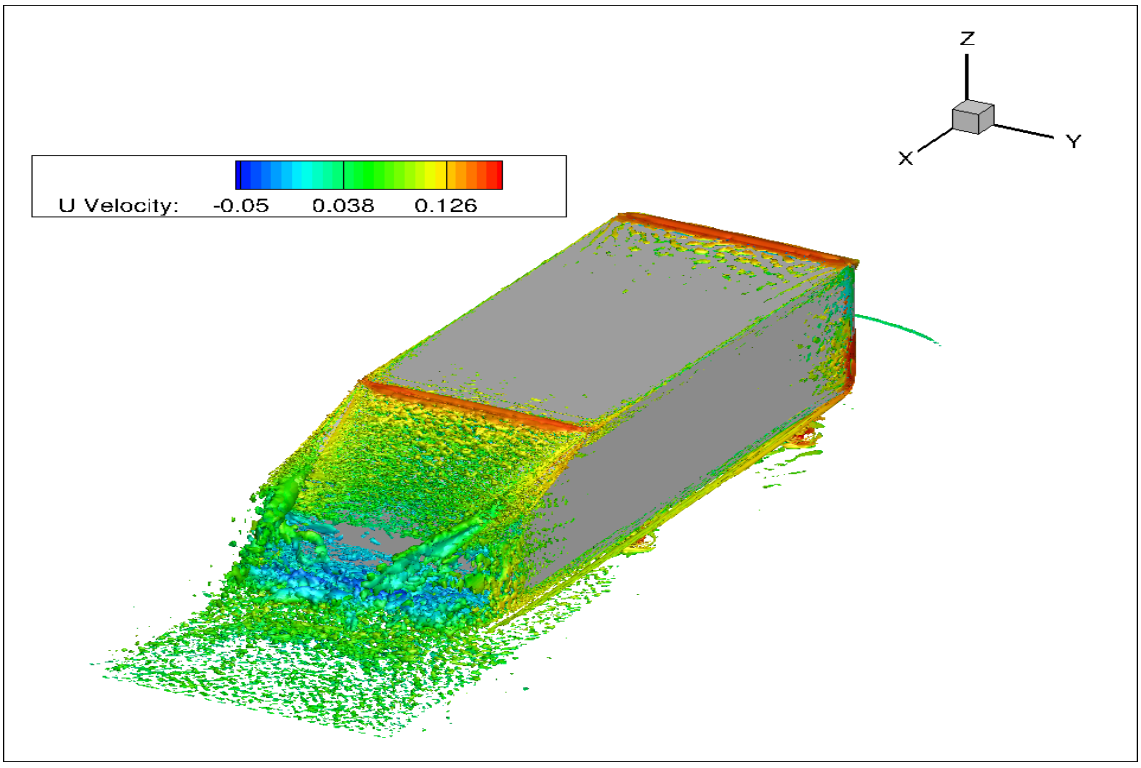

Figure 4.27: λ-2 Criterion at -1 x 10^{-6} for URANS simulation at $\phi = 25°$ colored by streamwise velocity

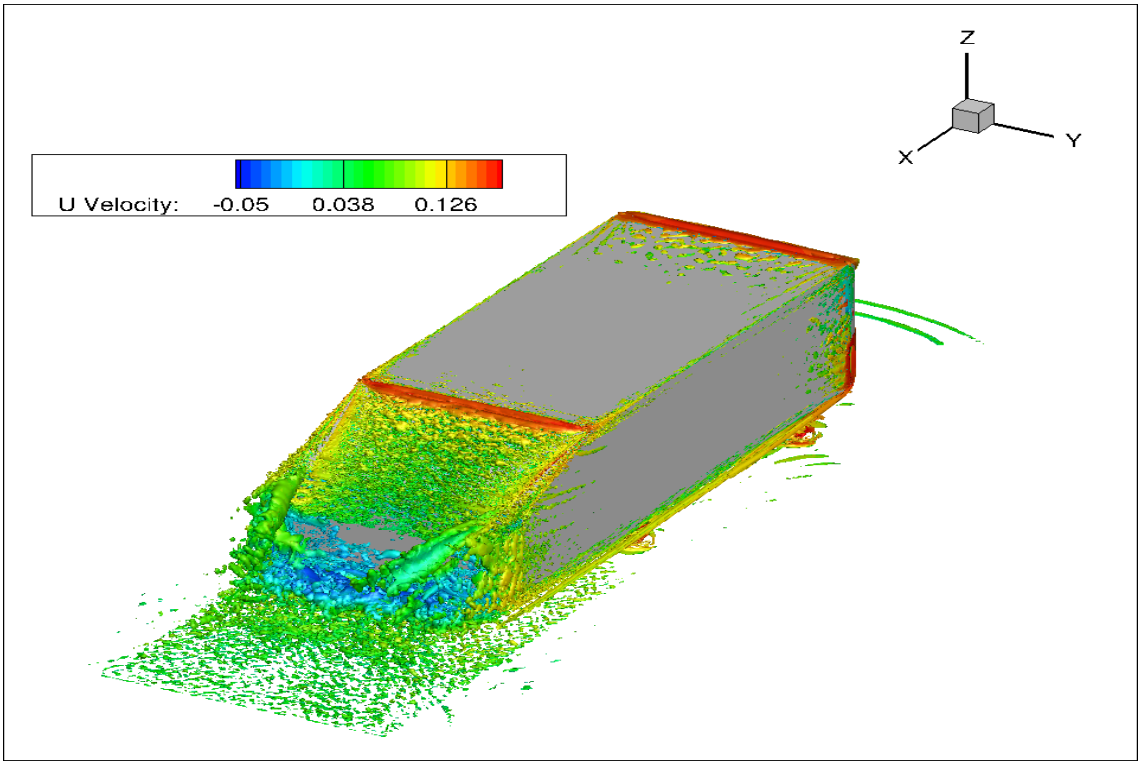

λ-2 Criterion at -1 x 10^{-6} for URANS simulation at $\phi = 25°$ colored by streamwise velocity

Angle	Experiment [2]	SST DDES Original Grid	SST DDES Elongated Grid
25	0.298	0.303	0.280
35	0.255	0.262	0.238

Table 4.13: Comparison of original grid SST-DDES C_D coefficients with the modified grid

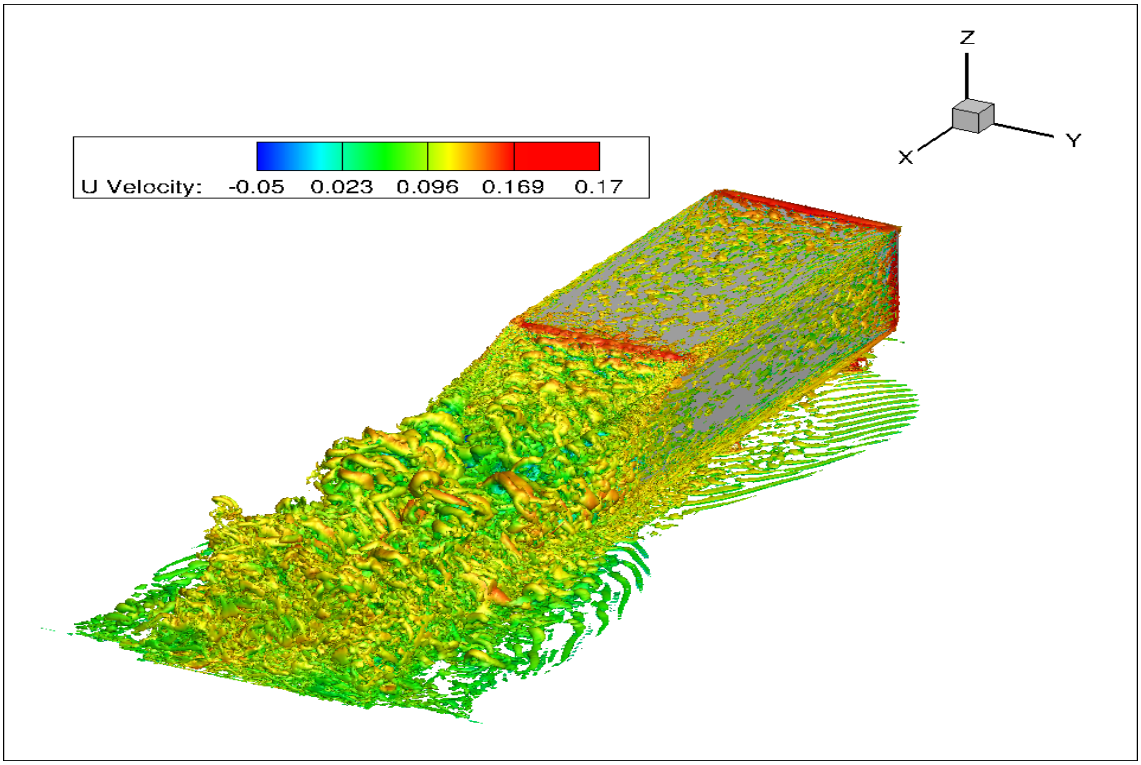

Figure 4.28: λ-2 Criterion at -1 x 10^{-6} showing the extended region of refinement and turbulence of the flow (0.05 seconds)

new extended mesh. The differences between the flow fields of the original grid and elongated grid are minimal except for the increased resolution within the wake further into the far field. The recirculation area is fully enclosed within the refinement of the original grid and only the vortex shedding in the far field has increased resolution. For both grid the C_D has decreased roughly twenty counts possibly due to CFD predicting better pressure recovery within the wake. The C_L for the sub-critical angle changes slightly, while the super-critical angle does not predict the lift as well, but is still directionally correct.

These elongated simulations were run for the minimum amount of time to provide

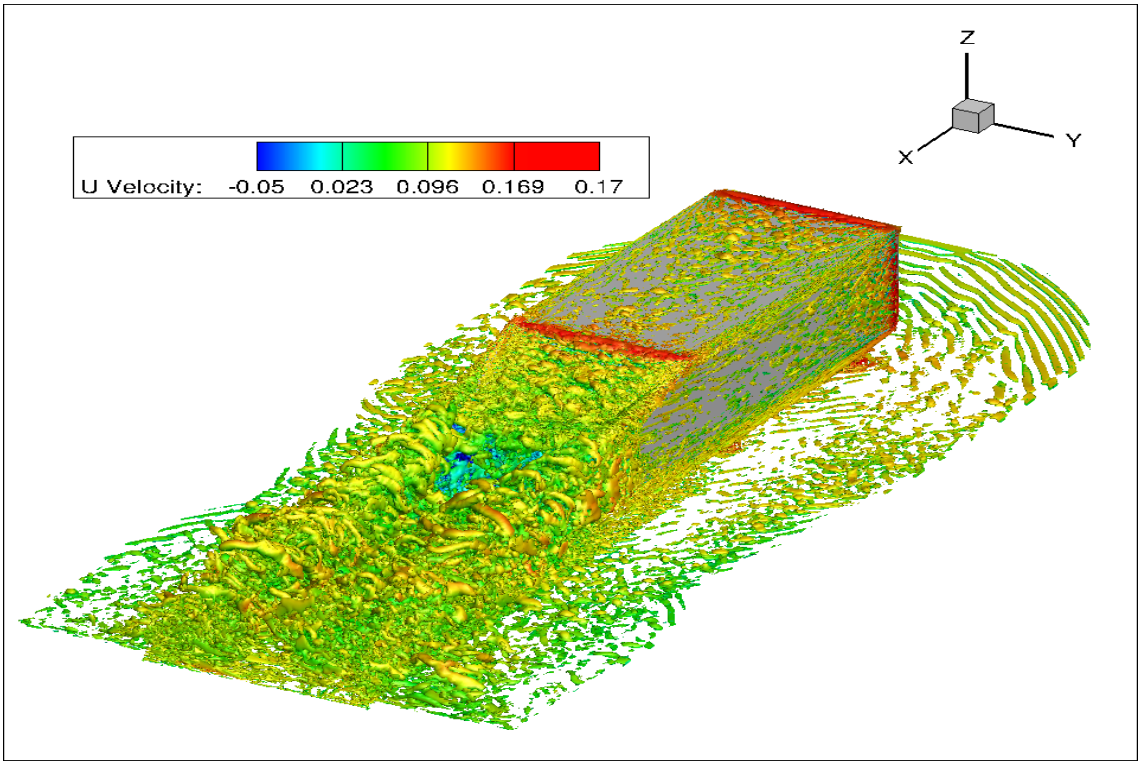

Figure 4.29: λ-2 Criterion at -1 x 10^{-6} showing the changes to the flow at a different time step (0.08 seconds)

Angle	Experiment [7]	SST DDES Original Grid	SST DDES Elongated Grid
25	0.315	0.282	0.286
35	-0.050	-0.055	-0.014

Table 4.14: Comparison of original grid SST-DDES C_L coefficients with the modified grid

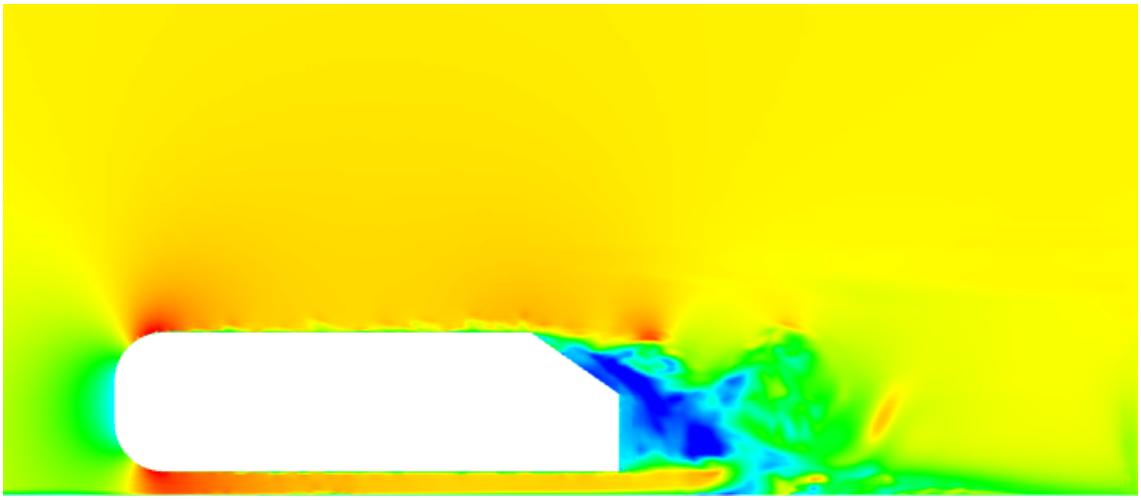

Figure 4.30: Unsteady Streamwise velocity of SA-DDES simulation at $\phi = 25°$

accurate drag results, which appears to be true since their errors are within those predicted on the original mesh. The time to provide steady C_L values takes longer than the simulation time therefore these numbers could improve with further simulation time. These simulations would be an excellent further study to look at the effects of the far field wake as the vortex shedding dissipates.

4.5 Comparison of Two Turbulence Models

A popular turbulence model used for lifting bodies and wings is the Spalart-Allmaras (SA) one-equation turbulence model. Its efficiency and ability to solve the flow on adverse pressure gradients is a strength of the model. Some attempts to use the model have been made in road-vehicle flows, but since the model was developed for attached flow the large areas of separation give this model difficulty [12]. Even though this model has been improved for RANS/LES methods, it still has difficulties predicting the flow field and forces for the bluff body aerodynamic simulations. This model was tested on both the sub and super-critical angles with the elongated mesh within the rear wake in to attempt and improve the predictions of C_L for this simple geometry.

Predictably the SA model did not predict either C_D or C_L well and failed to

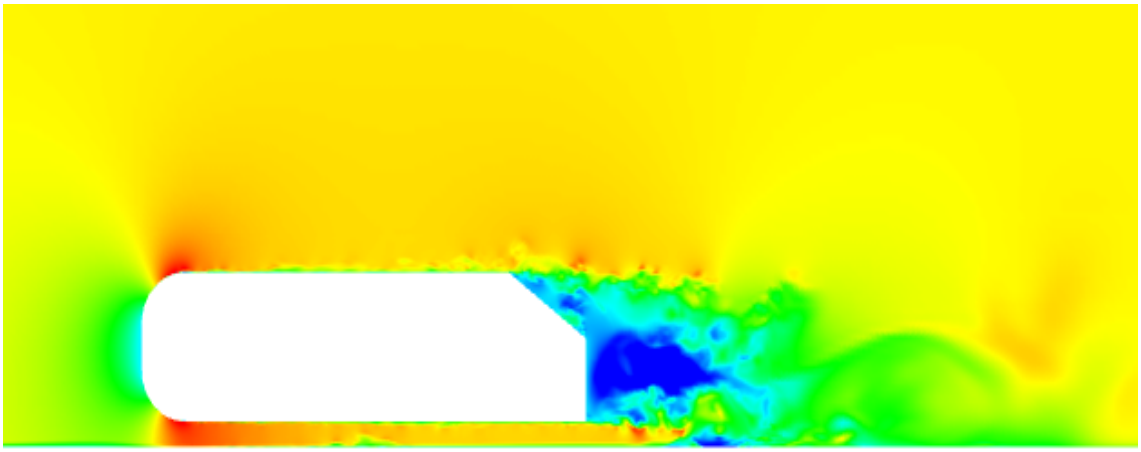

Figure 4.31: Unsteady Streamwise velocity of SA-DDES simulation at $\phi = 35°$. Notice the low velocity along the rear slant suggesting the flow is still attached at the super-critical angle

Angle	Experiment [2]	SA DDES Elongated Grid	SST DDES Elongated Grid
25	0.298	0.319	0.280
35	0.255	0.366	0.238

Table 4.15: Comparison of SA-DDES C_D coefficients with those of SST-DDES

predict the separation shown at the super-critical angle instead predicting two large recirculation areas, one after the corner junction and one behind the wake of the body (Figure 4.31). Further analysis on the unsteady structures would not give any new insights to the flow around a generic simplified car body since the results are unphysical and therefore were not performed.

Angle	Experiment [7]	SA DDES Elongated Grid	SST DDES Elongated Grid
25	0.315	0.377	0.286
35	-0.050	0.283	-0.014

Table 4.16: Comparison of SA-DDES C_L coefficients with those of SST-DDES

CHAPTER 5: CONCLUSIONS

The simulations that were conducted throughout this study tested the abilities of the finite-difference code OVERFLOW and looked into providing high-order simulation results for flow past a generic simplified car model. This thesis concluded that the methods used to predict drag coefficients are consistent with the multitudes of experimental data available and were also a good match for the flow fields, suggesting that this method could be applied to more complex models. While this thesis provided a methodology for more realistic simulations, its attempt to make an improvement upon the prediction of lift coefficients was inconclusive.

Through the GCI simulations, no grid predicted a C_L value where experimental error and mesh error overlapped. The value for C_L on the largest grid was only extrapolated for DES simulations. Additionally, the GCI study only studied the convergence of the solution at the 25° rear slant angle for C_D values, which effectively tuned the simulation towards this specific configuration. These conditions created the optimal grid size at 57 million nodes, but accounting for the differences through all of the subsequent simulations and the lack of accuracy in C_L, a slightly higher mesh count would have resulted in better results. Further GCI studies should be run for multiple different configurations measuring multiple forces on the body before deciding the optimal grid is best to continue subsequent studies upon. Additional optimization methods could also be explored within further studies to enhance the speed of the simulations.

The CFD predictions of C_D compared relatively well to the experimental values presented by Ahmed and Leinhart for various slant angles and the C_L were predicted

further from their experimental counterparts. The ultimate tuning of the simulation towards the $\phi = 25°$ case turned up within these various configurations as well since the body forces were well predicted at this condition and varied elsewhere. The predictions of C_L in the supercritical angle range were inconsistent even though the RANS simulation predicted the exact value. Since only one super-critical angle was tested, the overall trends of C_D and C_L within this range cannot be ascertained. Further testing at higher angles would be necessary to draw any meaningful conclusions at higher angles, but when $\phi = 25°$ the predictions of lift and drag forces were excellent.

CFD failed to predict the bifurcation of the flow at the critical angle when changing the rear slant angle. This can be attributed to modelling errors and limiting of the turbulent kinetic energy at the critical angle, therefore, limiting the ability for the critical angle to switch between reattaching down the body and separating at the leading edge. Testing larger a_1 coefficients in the Menter SST model will increase the maximum turbulent kinetic energy, where at a certain value the bifurcation should be present. Additionally, rounding the junction between the top and the rear slant may better represent the physical model since minor deviations can prevent the flow from separating, while the CFD model has a precise discontinuity within this area.

There was little data for Strouhal numbers within the wake and along the rear slant for angles where $\phi \neq 25°$, but at the sub-critical angle the predictions of the Strouhal number were close to experimental data, regardless of the Reynolds number or solver method. Within the wake the results were not as close to experimental results, which were expected, because in this region is where the Strouhal number is very dependent upon the Reynolds number. In bulk magnitude the approximations with the empirical solution to the Strouhal number based upon C_D the predicted results were very similar and provided the best comparisons at all rear slant angles.

Since comparing the solver methods were done on a grid tuned to the specific configuration, all models predicted C_D extremely close to the experimental data and

all C_L values were predicted close to each other. All flow fields also provide similar results and resolves similar structures among the various solvers, where the DDES solver appears to not only be faster than URANS solutions, but also predict C_L the better. Increasing the prediction of C_L would require overall more mesh refinement.

Increasing the length of the refined mesh settings rearward, further beyond the model, did not improve the body forces, but gives a better insight to the flow behind the body. Unsteady analysis in the far field were not conducted, but would yield interesting results for multi body simulations. Finally using various two-equation turbulence models may provide more accurate or beneficial results, which would be easy to test, but running the Spalart-Allmaras turbulence model resulted in simulations that predicted neither the body forces correctly nor the flow field.

Simple optimizations could further enhance these simulations, but the basic modelling technique and simulation setup yields fairly accurate results on a stationary simplified generic car model. As a simple simulation to test a different direction for acquiring CFD predictions, the high-order finite-difference method provided accurate results for both steady and unsteady simulations, but also shows small weaknesses of the process used within this thesis that could be easily rectified. Depending on the scope of the realistic problem, both of these methods could be easily implemented for road vehicle aerodynamic simulations.

5.1 Future Research

While there is an extraordinary amount of research associated with generic car models, this particular thesis did not address many fundamental key features that could enhance efficiency or accuracy of the solution.

A first step would be to attempt to optimize both the mesh and solver settings in order to decrease the computational time needed to complete an unsteady simulation without sacrificing accuracy. Simple steps from here will increase the productivity of research with the OVERFLOW code and solutions that work for the generic car

model could be applied to more complex models efficiently.

5.1.1 DNS Simulation

The simplicity of the generic simplified car model makes it a good candidate to test for a direct numerical simulation (DNS). The simulations within this study were extremely large with a very fine grid spacing and wall spacing in order to test the effects of steady and unsteady simulations with RANS and hybrid RANS/LES equations. While the correlations are decent, although lacking in predicting C_L, it was predicted that running the largest grid would produce lift coefficients that were within the experimental error. The ultimate goal is to run a CFD without using turbulence models and therefore avoid correlation issues since there is no turbulent modelling during a direct numerical simulation. While possible there are some changes to be made before this simulation can be run as a DNS case.

In order to run DNS, the current mesh setup would have to be slightly modified in order to remove all orphan points around the feet to avoid the solution blowing up prematurely. Using the Kolmogorov microscales (Equations (5.1), (5.2), and (5.3)) an estimate for the maximum velocity and Reynolds number can be obtained.

$$\eta = \left(\frac{\nu^3}{\epsilon}\right)^{(\frac{1}{4})} \tag{5.1}$$

$$u_\eta = (\nu\epsilon)^{(\frac{1}{4})} \tag{5.2}$$

$$\tau_\eta = \left(\frac{\nu}{\epsilon}\right)^{(\frac{1}{2})} \tag{5.3}$$

Assuming that the Kolmogorov length scale (η) is the smallest scale on the grid then with the current setup, the generic simplified car model could be run at Re = 28900, or approximately 1.4 m/s. Unfortunately assuming the numerical scheme to

solve the equations has a maximum CFL number of 1 for stability, 500 x 10^6 time steps are necessary in order to run the simulation at the same length as the previous simulations. This number could be decreased depending upon the maximum CFL number for stability, which could be easily tested on a smaller scale.

The simplicity of the Ahmed Body makes it an excellent candidate to start doing initial DNS simulations. At the largest model size that was run within this paper, the Reynolds number is within the threshold of turbulent flow and can become an initial object to look at a more complex bluff body for DNS studies instead of simpler geometric objects.

5.1.2 More Complex Models

Instead of doing more fundamental research on the physics of the flow around generic simplified car models, more complex bodies could be simulated with similar procedures used within this paper. The most logical decision would be to start with the DrivAer Model. This was already tested within OVERFLOW by Peters *et. al.* and adjustments could be made to run unsteady flow problems around the body[52]. With the additional complexity of this body, a mesh study would be suggested along with the addition of writing a rolling road boundary condition to further mimic the experiment.

In addition to a realistic model, dynamic simulations could be created where the model pitches, rolls, and heaves. While difficult to setup and simulate, the difficult portion of these complex transient models is the ability to compare directly with experimental results. Ultimately the complexity of these simulations should expand to accurately modelled race cars performing dynamic movements, giving insight to how these complex systems evolve during primary vehicle movements.

BIBLIOGRAPHY

[1] Ahlborn, B., Seto, M. L., and Noack, B. R., "On drag, Strouhal number and vortex-street structure," Fluid Dynamics Research, March 2002

[2] Ahmed, S.R., Ramm, G., and Faltin, G., "Some Salient Features of the Time-Averaged Ground Vehicle Wake," March 1984, SAE Technical Paper 840300

[3] Ascher, U. M., and Petzold, L. R., "Computer methods for ordinary differential equations and differential-algebraic equations," Vol 61, Siam, 1998

[4] Ashton, N., West, A., Lardeau, S., and Revell A., "Assessment of RANS and DES methods for realistic automotive models," January 2016, Computers and Fluids, 2016

[5] Ashton, N., and Revell, A., "Key factors in the use of DDES for the flow around a simplified car," June 2015, International Journal of Heat and Fluid Flow

[6] Aljure, D. E., Lehmkul, O., Rodriguez I., Oliva, A., "Flow and turbulent structures around simplified car models," March 2014, Computers and Fluids

[7] Baxendale, A. J., Graysmith, J. L., Howell, J. P., and Haynes T., "Comparisons between CFD and experimental results for the Ahmed reference model," RAeS Conference on Vehicle Aerodynamics, pp 30-1, 1994

[8] Bayraktar, I., Landman, D., and Baysal O., "Experimental and computational investigation of Ahmed body for ground vehicle aerodynamics," SAE paper 2001-01-2742, 2001

[9] Benedict, L. H., Gould R. D., "Towards better uncertainty estimates for turbulence statistics," 1996, Experiments in Fluids, 22, 129-136

[10] Blevins, R. D., *Flow-Induced Vibration* 2nd Ed. New York, New York, Van Nostrand Reinhold Co., Inc, 1990-01-01, 1990

[11] Chan, W. M., Gomez, R. J., Rogers, S. E. and Buning, P. G., "Best Practices in Overset Grid Generation," 32nd AIAA Fluid Dynamics Conference, St. Louis, Missouri, June, 2002, AIAA-2002-3191

[12] Collie, S. J., Gerritsen, M., and Jackson, P., "A Review of Turbulence Modelling for use in Sail Flow Analysis," 2001, School of Engineering Report, No. 603

[13] Debien, A., Aubrun, S., Mazellier, N., and Azeddine, K., "Active Separation Control Process Over a Sharp Edge Ramp," International Symposium on Turbulence and Shear Flow Phenomena, Melbourne, Australia, July 3, 2013

[14] Eberly, D., "Derivative Approximation by Finite Differences," Magic Software, Inc, 2008

[15] Evans, S., Lardeau, S., and Pettineli, C., "Validation of a turbulence methodology using the SST $k-\omega$ model for adjoint calculation," 54th AIAA Aerospace Sciences Meeting, 2016

[16] Fares, E., "Unsteady flow simulation of the Ahmed reference body using a lattice Boltzmann approach," April 2005, Computers and Fluids

[17] Fourrie, G., Keirsbulck, L., Labraga, L., "Wall shear stress characterization of a 3D bluff-body separated flow," May 2013, Journal of Fluids and Structures

[18] Gritzkevich, M. S., Garbaruk, A. V., Schutze, J., and Menter, F. R., "Development of DDES and IDDES Formulations for the k-ω Shear Stress Transport Model," 2011, Flow Turbulence Combust, Vol 88, DOI 10.1007/s10494-011-9378-4

[19] Gulyas, A., Bodor, A., Regert, T., Janosi I., "PIV measurement of the flow past a generic body with wheels at LES applicable Reynolds number," July 2013, International Journal of Heat and Fluid Flow

[20] Haller, G., "An objective definition of a vortex," Journal of Fluid Mechanics 525, p1-26, 2005

[21] Heft, A., Indinger, T., and Adams, N., "Introduction of a New Realistic Generic Car Model for Aerodynamic Investigations," SAE Technical Paper 2012-01-0168, 2012, doi:10.4271/2012-01-0168

[22] Holmen, V., "Methods for Vortex Identification," Master's Theses in Mathematical Sciences, 2012.

[23] Jespersen, D., Pulliam, T., and Buning P., "Recent Enhancements to OVERFLOW," 1997, AIAA-97-0644

[24] Jeong, J., Hussain, F., "On the identification of a vortex," Journal of Fluid Mechanics, pp. 69-94, 1995,

[25] Jimenez, J., "The contributions of A. N. Kolmogorov to the theory of turbulence," August 2004, Arbor, pp 589-606, 2004

[26] Kalitzin, G., Medic, G., Iaccarino, G., and Durbin, P., "Near-Wall behavior of RANS turbulence models and implications for wall functions," June 2004, Journal of Computational Physics, 2005

[27] Kourta, A., Thacker, A., Joussot, R., "Analysis and characterization of ramp flow separation," April 2015, Experiments in Fluids,

[28] Leinhart, H., Becker, S., "Flow and turbulence structure in the wake of a simplified car model," SAE Paper, 2003-01-0656, 2003

[29] Leinhart, H., Stoots, C., Becker, S., "Flow and turbulence structures in the wake of a simplified car model (Ahmed Body)," DGL fach symposium der AG STAB, Stuttgart university, November 2000

[30] Martin-Alcantara, A., Sanmiguel-Rojas, E., Gutierrez-Montes, C., Martinex-Bazan, C., "Drag reduction induced by the addition of a multi-cavity at the base of a bluff body,"

[31] McCorquodale, P., and Colella, P., "A High-Order Finite-Volume Method for Conservation Laws on Locally Refined Grids," Common Applications of Math and Computer Science, 2011

[32] Meile, W., Brenn, G., Reppenhagen, A., Lechner, B., and Fuchs, A., "Experiments and numerical simulations on the aerodynamics of the Ahmed Body," September 2010, CFD Letters

[33] Meile, W., Ladinek, T., Brenn, G., Reppenhagen, A., Fuch, A., "Non-symmetric bi-stable flow around the Ahmed body," November 2015, International Journal of Heat and Fluid Flow

[34] Menter, F., Kuntz, M., "Adaptation of Eddy-Viscosity Turbulence Models to Unsteady separated Flow Behind Vehicles," Ansys-CFX

[35] Menter, F., Kuntz, M., "Development and application of a Zonal DES-SST turublence model for CFX-5," CFX internal rep, Otterfing, Germany, 2003

[36] Menter, F. R., Kuntz, M., and Langtry, R., "Ten Years of Inudstrial Experience with the SST Turbulence Model," 2003, Turbulence Heat and Mass Transfer

[37] Minguez, M., Pasquetti, R., and Serre, E., "High-order large-eddy simulation of flow over the "Ahmed body" car model," May 2008, Physcis of FLuids 095101. 2008.

[38] Morel T., "The Effect of Base Slant on the Flow Pattern and Drag of three-dimensional Bodies with Blunt Ends, Proceedings of Symposium on Aerodynamic Drag Mechanisms of Bluff Bodies and Road Vehicles, 1978

[39] Nguyen, V., Nguyen H., "Detached eddy simulations of flow induced vibrations of circular cylinders at high Reynolds numbers," February 2016, Journal of Fluids and Structures

[40] Nichols, R., Buning, P., "User's Manual for OVERFLOW 2.2: Version 2.2l, February 2016," http:/www.overflow.larc.nasa.gov/home/users-manual-for-overflow-2-2/

[41] Paik, J., Escauriaza, C., and Soitropoulos, F., "On the bimodal dynamics of the turbulent horseshoe vortex system in a wing-body junction," 2007, Physics of Fluids

[42] Pandya, S. A., Venkateswaran, S., and Pulliam, T. H., "Implementation of Preconditioned Dual-Time Procedures in OVERFLOW," 2003, AIAA-2003-0072

[43] Roache, P. J., "Quantification of Uncertainty in Computational Fluid Dynamics," 1997, Annual Review of Fluid Mechanics, 1997.29:123-160

[44] Roshko, A., "On the drag and shedding frequency of two-dimensional bluff bodies," Technical Report TN 1191, NACA, US Government Printing Office, Washington, DC, 1954

[45] Schewe, G., "Sensitivity of the transition phenomena to small perturbations in flow round a circular cylinder," Journal of Fluid Mechanics, 172, 33-46, 1986

[46] "Is your Mesh Refined Enough?" Estimating discretization error using GCI. LSDYNA User Forum, Banberg Germany, 2008

[47] Schmidt, H. J., Woszidlo, R., Nayeri, C. N., Paschereit, C. O., "Drag reduction on a rectangular bluff body with base flaps and fluidic oscillators," June 2015, Experiments in Fluids

[48] Serre, E., Minguez, M., Richard, P., Guilmineau, E., Deng, G., Kornhaas, M., Schafer, M., Frohlich, J., Hinterberger, C., Rodi, W., "On simulating the turbulent flow around the Ahmed body: A French-German collaborative evaluation of LES and DES," May 2011, Computers and Fluids

[49] Shu, C., "High Order Finite Difference and Finite Volume WENO Schemes and Discontinuous Galerkin Methods for CFD," International Journal of Computational Fluid Dynamics, 17.2, 2003

[50] Spalart, P. R., Deck, S., Shur, M. L., Squires, K. D., Strelets, M. Kh., and Travin, A., "A new version of detached-eddy simulation, reistant to ambiguous grid densities," May 2006, Theoretical Computational Fluid Dynamics, doi 10.1007/s00162-006-0015-0

[51] Perry, A. K., Almond, M., Passmore, M., and Littlewood, R., "The Study of a Bi-Stable Wake Region of a Generic Squareback Vehicle using Tomographic PIV," SAE International Journal of Passenger Cars-Mechanical Systems, 2016-01-1610, 2016

[52] Peters, B. C., Uddin, M., Bain, J., Curley, A., and Henry, M. L., "Simulating DrivAer with Structured Finite Difference Overset Grids," SAE Technical Paper, 2015-01-1536, 2015

[53] Pulliam, T. H., "Solution Methods In Computational Fluid Dynamics," Notes for the von Karman Institute For Fluid Dynamics Lecture Series, 1986

[54] Thacker, A., Aubrun, S., Leroy, A., Devinant, P., "Unsteady analyses of the flow separation on the rear window of a simplified ground vehicle model," June 2010, AIAA Applied Aerodynamics Conference, Chicago, Illinois, 2010

[55] Tritton, D. J., "Experiments on the flow past a circular cylinder at low Reynolds numbers," Journal of Fluid Mechanics, Vol. 6, pp 547 - 567, Cambridge University Press, 1959

[56] Venning, J., Jacono, D. L., Burton, D., Thompson, M., Sheridan, J., "The effect of aspect ratio on the wake of the Ahmed body," May 2015, Experiments in Fluids

[57] Vino, G., Watkins, S., Mousley, P., Watmuff, J., Prasad, S., "Flow structures in the near-wake of the Ahmed model," March 2005, Journal of Fluids and Structures

[58] Watkins, S., Vino, G., "The effect of vehicle spacing on the aerodynamics of a representative car shape," August 2007, Journal of Wind Engineering

[59] White, F. M., "Viscous Fluid Flow," McGraw Hill, Inc., New York, 1974

[60] Wood, D., Passmore, M. A., and Perry A. K., "Experimental data for the validation of Numerical Methods - SAE Reference Notchback Model," SAE Technical Paper 2014-01-0590, 2014

[61] Zhang, B. F., To, S., and Zhou, Y., "Strouhal Numbers of Unsteady Flow Structures Around a Simplified Car Model," 2014

[62] http:/www.ercoftac.org/finadmin/userupload/bigfiles/sig15/database/index.html

[63] http:/www.chevyhardcore.com/new/a-look-at-chevrolets-new-indycar-aero-kits/